Spectral analysis of near-wall turbulence in channel flow at $\mathrm{Re}_\tau = 4200$ with emphasis on the attached-eddy hypothesis

Lionel Agostini*
Department of Mechanical and Aerospace Engineering, The Ohio State University Columbus, Ohio 43210, USA
and Department of Aeronautics, Imperial College London, South Kensington, London SW7 2AZ, United Kingdom

Michael Leschziner†
Department of Aeronautics, Imperial College London, South Kensington, London SW7 2AZ, United Kingdom
(Received 1 August 2016; published 18 January 2017)

Direct numerical simulation data for channel flow at a friction Reynolds number of 4200, generated by Lozano-Durán and Jiménez [J. Fluid Mech. **759**, 432 (2014)], are used to examine the properties of near-wall turbulence within subranges of eddy-length scale. Attention is primarily focused on the intermediate layer (mesolayer) covering the logarithmic velocity region within the range of wall-scaled wall-normal distance of 80–1500. The examination is based on a number of statistical properties, including premultiplied and compensated spectra, the premultiplied derivative of the second-order structure function, and three scalar parameters that characterize the anisotropic or isotropic state of the various length-scale subranges. This analysis leads to the delineation of three regions within the map of wall-normal-wise premultiplied spectra, each characterized by distinct turbulence properties. A question of particular interest is whether the Townsend-Perry attached-eddy hypothesis (AEH) can be shown to be valid across the entire mesolayer, in contrast to the usual focus on the outer portion of the logarithmic-velocity layer at high Reynolds numbers, which is populated with very-large-scale motions. This question is addressed by reference to properties in the premultiplied scalewise derivative of the second-order structure function (PMDS2) and joint probability density functions of streamwise-velocity fluctuations and their streamwise and spanwise derivatives. This examination provides evidence, based primarily on the existence of a plateau region in the PMDS2, for the qualified validity of the AEH right down the lower limit of the logarithmic velocity range.

DOI: 10.1103/PhysRevFluids.2.014603

I. INTRODUCTION

The Townsend-Perry attached-eddy hypothesis (AEH) [1–3] is one of the major historical fixed points of sheared near-wall turbulence. Its most important statistical constituent is the statement that the energy-containing motions in the logarithmic layer are associated with coherent eddies that are attached to the wall, both their dimension and their energy rising linearly with wall distance, implying that the eddies are self-similar. Perry *et al.* [3] thus proposed a conceptual model of a hierarchy of wall-attached eddies that increase in size by consecutive doubling and span the entire boundary layer, from the viscous scale $\delta_\nu = \nu/u_\tau$ to the outer edge δ.

The AEH is compatible with two principal statistical characteristics. One, derived by Townsend [1], is that the streamwise and spanwise turbulence-energy components $\overline{u'u'}$ and $\overline{w'w'}$, respectively, decay logarithmically towards the edge of the velocity logarithmic layer. Another is that the energy

*l.agostini@imperial.ac.uk
†mike.leschziner@imperial.ac.uk

spectra, within the logarithmic range of the energy components, follow the law $E_{uu}(k_x) \propto k_x^{-1}$ and $E_{ww}(k_x) \propto k_x^{-1}$, i.e., that the premultiplied spectra assume a constant value [3–5]. Integration of these spectra with respect to k_x (or its inverse, the wavelength) then readily yields the logarithmic variation of the related turbulence-energy components.

As the presence of k_x^{-1} variation is not easily identifiable, at least in one-dimensional spectra at moderate-Reynolds-number values, Davidson *et al.* [6,7] proposed that the second-order structure function $S_{2,u}(\delta_x) = \langle [u(x+\delta_x) - u(x)]^2 \rangle$ should provide a more sensitive indicator of the validity of the AEH. Davidson *et al.* show that the behavior is consistent with a logarithmic rise of $S_{2,u}(\delta_x)$ up to the integral length scale, beyond which the structure function tends to a constant value. When the structure function is scaled with the squared of the shear velocity u_τ^2 and δ_x is scaled with y, the expectation is that it should display a universal behavior, independent of the wall distance y, and this is indeed demonstrated by Davidson *et al.* [6,7] for two particular boundary layers at momentum-thickness Reynolds-number values $\mathrm{Re}_\theta = 12\,600$ and 37 500, the latter corresponding to $\mathrm{Re}_\tau \approx 14\,000$. A focus on $S_{2,u}(\delta_x)$, as a diagnostic indicator of wall-normal eddy organization and the AEH, was most recently advocated by de Silva *et al.* [8] and Chung *et al.* [9], the former analyzing the structure of boundary layers at Re_τ up to approximately 10^6 and the latter aimed primarily at reconciling significant differences between high-Reynolds-number boundary-layer and pipe-flow data with respect to the k_x^{-1} region in the associated spectra. In common with most studies examining aspects of the AEH, de Silva *et al.* [8] concentrate their attention on the outer portion of the respective boundary layers, beyond the position of the plateau (or second maximum) in the wall-normal variation of the streamwise turbulence-energy component, where the second-order structure function varies logarithmically with the two-point separation and where the variations collapse if this separation is normalized by the wall distance. Based on theoretical considerations by Woodcock and Marusic [10], who provide formal support and an analytical model for the AEH, de Silva *et al.* [8] also extend their investigation to higher-order structure functions and demonstrate a logarithmic-scaling behavior for these functions at sufficiently-high-Reynolds-number values and a separation distance larger than the wall distance.

Townsend's and Perry's original interpretation was that the AEH applies to the entire velocity logarithmic-law region. Studies consistent with this view are those of Davidson *et al.* [6,7] and Hwang [11]. The former discuss the logarithmic behavior of the structure function within the range $100 < y^+ < 200$, in relation to the k_x^{-1} behavior that is observed by Nickels *et al.* [5] to apply in the boundary layer at $\mathrm{Re}_\theta = 37\,500$ over a similar y^+ range. Analyzing the implications of a sequence of minimal-channel simulations, each used to isolate the characteristics of a narrow size ranges of eddies, Hwang [11] argues that the entire logarithmic-law layer is populated, as suggested by Jiménez and Hoyas [12] and Marusic *et al.* [13], by a hierarchical set of self-similar and self-sustaining attached eddies, in line with the original AEH. However, the above interpretation appears at odds with results derived from experimental data for high-Reynolds-number pipe flow [14,15] and also direct numerical simulation (DNS) data for channel flow at $\mathrm{Re}_\tau = 4200$ [16,17], which show that the logarithmic variation of $\overline{u'u'}^+$ does not apply across the intermediate portion of the velocity logarithmic-law layer, referred to as the mesolayer henceforth, which separates the layer below $y^+ \approx 100$ from the outer region lying beyond $y \approx 0.5\delta$ (around $y^+ = 2000$ in the channel flow considered herein). The reason is that the streamwise fluctuation-energy profile is increasingly affected, as the Reynolds number exceeds $\mathrm{Re}_\tau \approx 1000$, by contributions arising from energetic outer structures having streamwise and spanwise length scales of order 5δ–10δ and 0.5δ–1δ, respectively [18–20]. The wall-normal variation of the streamwise energy associated with these structures is fairly flat [21], increases with Re_τ, and its (weak) maximum is reported by Marusic *et al.* [22] to follow the location $y^+ \approx 3.9\sqrt{\mathrm{Re}_\tau}$ (corresponding to around 0.05δ). Importantly, the energy remains elevated well beyond this location, as well across the entire near-wall region including the mesolayer and indeed the viscosity-affected sublayer, causing substantial friction footprints on the wall; in other words, the energetic outer large-scale motions are highly correlated in the wall-normal direction. As a consequence, the energy profile no longer scales with u_τ and the logarithmic variation of $\overline{u'u'}^+$ in

the velocity logarithmic-law region is lost or becomes highly indistinct, at least at $\mathrm{Re}_\tau < 5000$. As observed by Vassilicos *et al.* [23], this behavior is incompatible with the AEH and this led them to propose a spectral range of the form $E_{uu} = Cu_\tau^2 \delta (k_x \delta)^{-m}$ for the intermediate range, allowing them to predict the rise in $\overline{u'u'}^+$ due to the outer scales.

Measurements at $\mathrm{Re}_\tau > 7000$ by Hutchins *et al.* [24], Hultmark *et al.* [14,25,26], and Rosenberg *et al.* [15] display a tendency for $\overline{u'u'}^+$ to reestablish a logarithmic-decay variation well beyond the mesolayer of the velocity logarithmic law and also well beyond the position of maximum large-scale energy, although with a slope different from that applicable within the velocity logarithmic-law layer at much-lower-Reynolds-number values. This has led to a proposition that the AEH should only apply in the extreme outer layer of the velocity logarithmic-law region, on the grounds that "determining the extent of the logarithmic layer from U^+ alone is difficult because of the slow departure from any log law" [27].

The evident controversy on the subject of the AEH, in particular, the wall-normal range to which it applies, motivated the present authors to examine the statistical properties of a channel flow at $\mathrm{Re}_\tau = 4200$. This value is substantially lower than that achieved in experiments, but is arguably high enough to undertake a searching study by postprocessing the highly resolved data that yield well-converged statistics. The DNS data were obtained with a spectral code by Lozano-Durán and Jiménez [16,17], according to well-established quality criteria, over a domain of $L_x = 2\pi h$ and $L_z = \pi h$, with a grid containing $3072 \times 3072 \times 1081$ nodes and cell dimensions $\Delta x^+ = 12.8$, $\Delta z^+ = 6.4$, and $\Delta y^+_{\max} = 10.7$. Downloaded data consisted of full-volume snapshot at 40 time levels, corresponding to 15 turnovers of the global eddies. While the motivation for the present study is rooted in, and emphasis is placed on, the AEH, the analysis extends, more broadly, to an examination of the statistical properties of, and scaling laws pertaining to, different scale subranges within the spectrum of turbulent fluctuations across the near-wall layer. Observations derived from the latter part turn out to be highly pertinent to the discussion on the validity of the AEH in the mesolayer.

II. STATISTICAL PROPERTIES OF EDDY-LENGTH-SCALE SUBRANGES

Figure 1 shows profiles of the streamwise turbulence energy for $\mathrm{Re}_\tau = 4200$ and 5200. The latter originates from a DNS study by Lee and Moser [28] for a channel flow performed over a box of $L_x = 8\pi h$ and $L_z = 3\pi h$, i.e., much larger than that exploited in the present study. Unfortunately, the raw data necessary for the analysis to follow are not available for the $\mathrm{Re}_\tau = 5200$ case.

Attention focuses here on what is termed the mesolayer, divided into two portions: the plateau region, covering $y^+ \approx 80$–500, and the outer layer, extending to around $y^+ \approx 2000$, i.e., roughly $0.5h$ in the present flow. The outer portion of the mesolayer, beyond the region in which the streamwise energy features an inflection region or a (second) maximum, is populated with very-large-scale motions and it is this layer that has been the focus of attention in studies of Vassilicos *et al.* [23], Marusic *et al.* [13], Hultmark *et al.* [14], and Rosenberg *et al.* [15], at $\mathrm{Re}_\tau > 7000$, who show that the streamwise energy displays a logarithmic-decay variation at the same slope as that in Fig. 1. The variation of the energy in the outer layer, $500 < y^+ < 1000$, suggests a logarithmiclike decay, especially at the high Reynolds value, and the slope of this decay is given in Fig. 1. Whether a logarithmic-decay law within the mesolayer is supported by other statistical properties will be examined below.

A property consistent with the logarithmic variation of $\overline{u'u'}^+$ and with the AEH is the presence of a region of constant value in the premultplied spectra $k_x \Phi_{uu}$, where x is assumed statistically homogeneous. If this region is bounded by $\lambda^+_{x,\,\min} = Cy^+$ and $\lambda^+_{x,\,\max} = \text{const}$, the logarithmic relationship emerges from

$$\overline{u'u'}^+(y^+) = \int_{\lambda^+_{x,\,\min}}^{\lambda^+_{x,\,\max}} k_x \phi_{uu}(y^+, \lambda_x^+) d\log(\lambda_x^+) = \int_{Cy^+}^{\text{const}} A d\log(\lambda_x^+) = -A\log(y^+) + B. \quad (1)$$

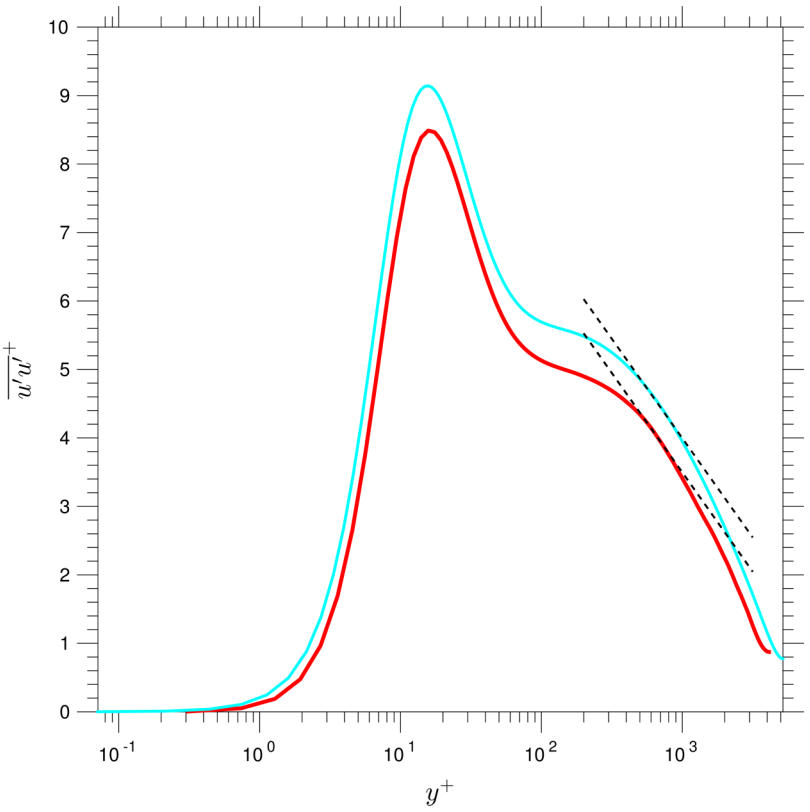

FIG. 1. Wall-normal distribution of the streamwise stress at $\mathrm{Re}_\tau = 4200$ (red line) and $\mathrm{Re}_\tau = 5200$ (blue line) from Lee and Moser [28]. The dashed lines represent the variation $\overline{u'u'}^+ = -1.26 \log y^+ + B$, with $B = 12.2$ and 12.7 for $\mathrm{Re}_\tau = 4200$ and $\mathrm{Re}_\tau = 5200$, respectively.

If, on the other hand, the upper limit of integration is a line parallel to that defining the lower limit, i.e., $\lambda_{x,\,\max}^+ = Dy^+$, then $\overline{u'u'}^+(y^+) = \text{const}$. The significance of this distinction between the two variations in the upper limits of integration will transpire in Sec. III. It is important to underline that, for the AEH to be valid, the equivalent of Eq. (1) must also apply with respect to the spanwise spectra, i.e., $k_z \Phi_{uu}$ must also be constant within boundaries corresponding to those applicable to the streamwise spectra.

Figure 2 shows the premultiplied spectra for $\mathrm{Re}_\tau = 4200$. Although there is an indication that the λ_x^+ and λ_z^+ locations at which the energy begins to rise steeply vary linearly with y^+, neither spectral maps features a well-defined constant-value plateau within the mesolayer, thus offering no obvious support for Eq. (1). A curious feature observed in Fig. 2(b) is the oscillatory behavior of the contours below and to the right of the red line, especially along the $y^+ - \lambda_z^+$ locus of maximum energy density. Although relatively mild, this behavior is indicative of a lack of convergence of the fast Fourier transform, an artifact that encourages the alternative use of the second-order structure function as a primary diagnostic means, pursued in Sec. III. The use of the structure function is also motivated by the fact that it is not affected by aliasing associated with the large-scale motion and thus leads to a better identification of the plateau region (see [6]). However, prior to this change in focus, the spectra, both those in Fig. 2 and others pertaining to the spanwise and wall-normal fluctuations, are used to examine some statistical properties of turbulence within different spectral portions of the eddy scales. The main objective is to identify and separate subranges of isotropic and anisotropic scales, the former characterizing the inertial subrange and associated with detached eddies [29] and

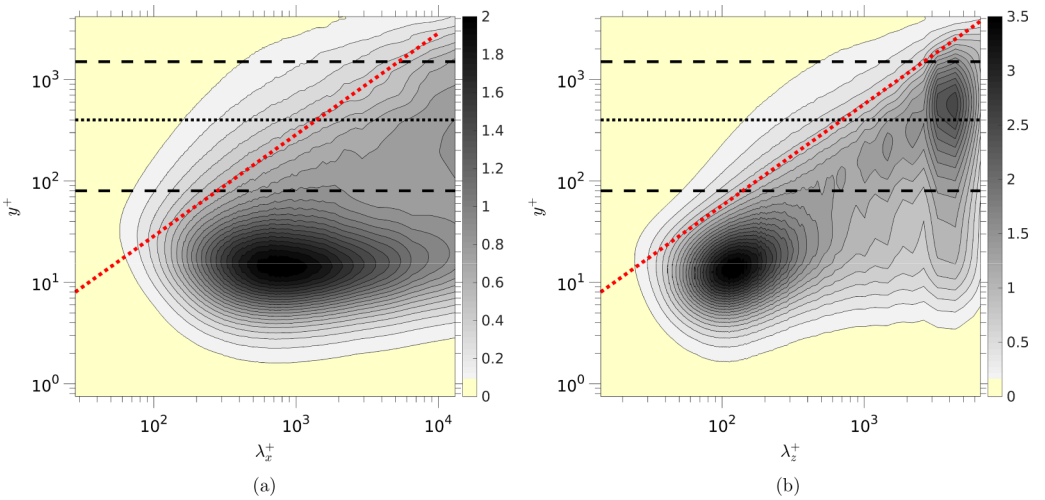

FIG. 2. Premultiplied power spectrum of the streamwise fluctuations in both the (a) streamwise and (b) spanwise directions at $\mathrm{Re}_\tau = 4200$. The dotted red lines show either the relation $\lambda_x^+ = 3.5y^+$ or $\lambda_z^+ = 7y^+ = 2\lambda_x^+$.

the latter, at larger scales, associated with attached eddies [3,6,30]. This identification is pursued below.

A. Inertial range: Detached eddies

In order to shed light on the characteristics of scale subranges, some specific manipulations of the spectral maps are proposed herein. Figure 3 shows two ways of highlighting the region in which the scales are close to being isotropic. The first entails the use of compensated spectra $\epsilon^{-2/3}k_x^{5/3}\Phi_{uu}$ and $\epsilon^{-2/3}k_z^{5/3}\Phi_{uu}$, which are shown Figs. 3(a) and 3(b), respectively, where ϵ is a surrogate of rate of turbulence-energy dissipation, defined such as $\epsilon = \overline{\omega_k\omega_k}/3$. The red lines in the x-wise and z-wise maps are defined, respectively, by $\lambda_x^+ = 3.5 \times y^+$ and $\lambda_z^+ = 7 \times y^+ = 2 \times \lambda_x^+$, while the blue lines describe, respectively, the variations $\lambda_x^+ = 3.5 \times (y^+)^{1/3}$ and $\lambda_z^+ = 7 \times (y^+)^{1/3} = 2 \times \lambda_x^+$. The red and blue lines bound, approximately, plateau regions characteristic of near isotropy.

The second route rests on the definition of the following isotropy parameter:

$$\gamma^{3c} \equiv \frac{3|\Phi_{uu}||\Phi_{vv}||\Phi_{ww}|}{|\Phi_{uu}|^3 + |\Phi_{vv}|^3 + |\Phi_{ww}|^3}, \tag{2}$$

in which Φ_{uu}, Φ_{vv}, and Φ_{ww} are the x-wise or z-wise spectra for the three components u, v, and w, respectively. This parameter tends to a maximum of 1 in the case of isotropy, declining to zero in the case of a two-component or a one-component state. The maps in Figs. 3(c) and 3(d) show (for greater visual impact) the square of γ^{3c} as functions of λ_x^+ and λ_z^+, respectively. The fact that regions of high γ^{3c} are again bounded by the red and blue lines and broadly coincide with the near-plateau regions in the compensated spectra supports the proposition that these regions within the mesolayer characterize detached eddies.

B. Anisotopic range: Attached eddies and large-scale motions

An analogous route to that taken in the previous section to highlight isotropy by use of the parameter γ^{3c} is adopted here to identify the region of elevated anisotropy. Thus, a parameter that

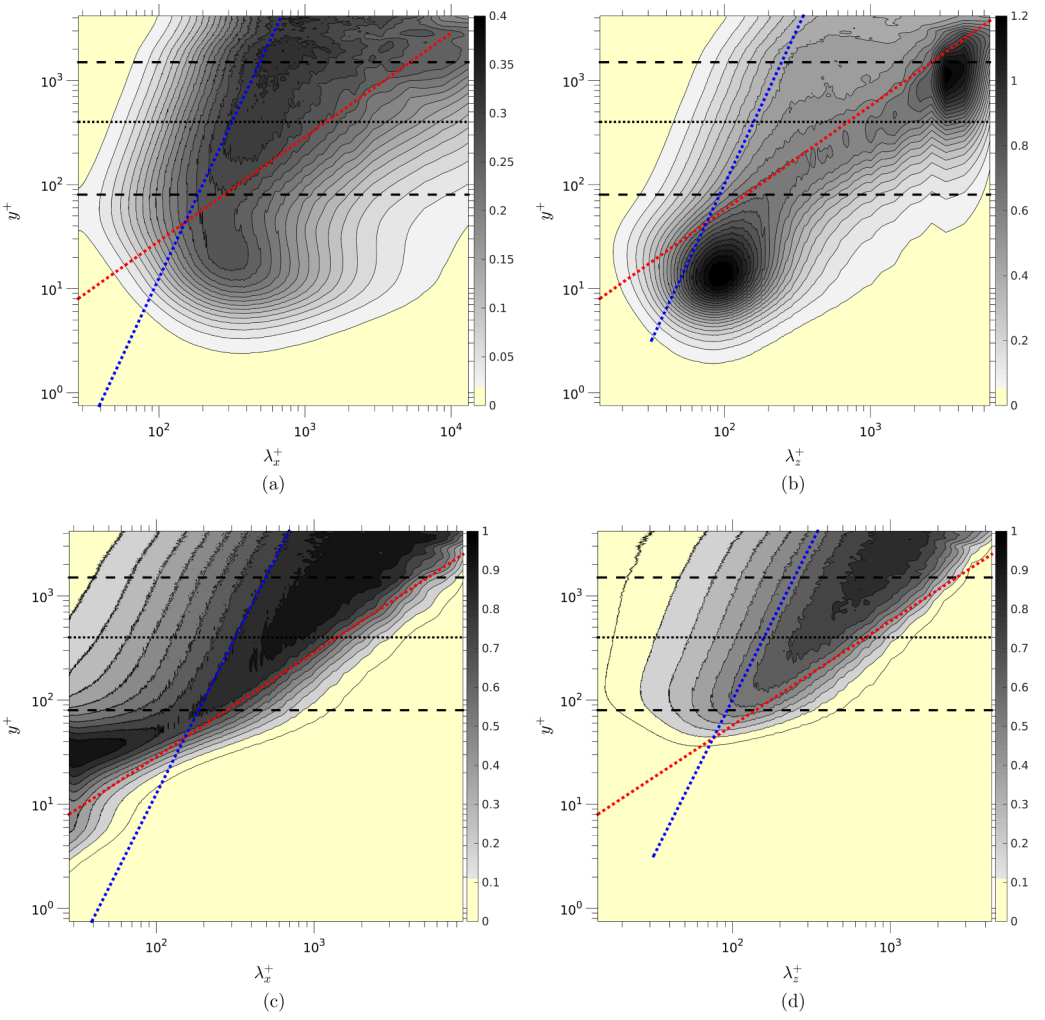

FIG. 3. Characterization of isotropy across eddy-size range: (a) compensated spectra $\epsilon^{-2/3}k_x^{5/3}\Phi_{uu}$, (b) compensated spectra $\epsilon^{-2/3}k_z^{5/3}\Phi_{uu}$, and (c) and (d) maps of the square of the isotropy parameter $(\gamma^{3c})^2$, derived from the streamwise and spanwise spectral components. The red lines show either the relation $\lambda_x^+ = 3.5y^+$ or $\lambda_z^+ = 7y^+ = 2\lambda_x^+$ and the blue lines show either the relation $\lambda_x^+ = 3.5(y^+)^{1/3}$ or $\lambda_z^+ = 7(y^+)^{1/3} = 2\lambda_x^+$.

identifies the dominance of the streamwise component over the two others is

$$\gamma_u^{1c} \equiv \frac{|\Phi_{uu}||\Phi_{uu}|}{|\Phi_{uu}|^2 + |\Phi_{vv}|^2 + |\Phi_{ww}|^2}. \tag{3}$$

This parameter tends to 1 when the energy is increasingly contained in the Φ_{uu} spectra and diminishes when the anisotropic state departs from the one-component condition. Maps of $(\gamma_u^{1c})^3$ in the x and z directions (the cubic exponent designed to accentuate gradients in the maps) are shown in Figs. 4(a) and 4(b), respectively.

Both maps reveal that, within the mesolayer, the dominance of the streamwise component is confined to the larger scales beyond the boundaries identified by the red lines and this is the attached-eddy region, as will be argued in Sec. III. In fact, the most pronounced regions in Fig. 4 pertain to scales that are the subject of many studies that deal with elongated large-scale structures in

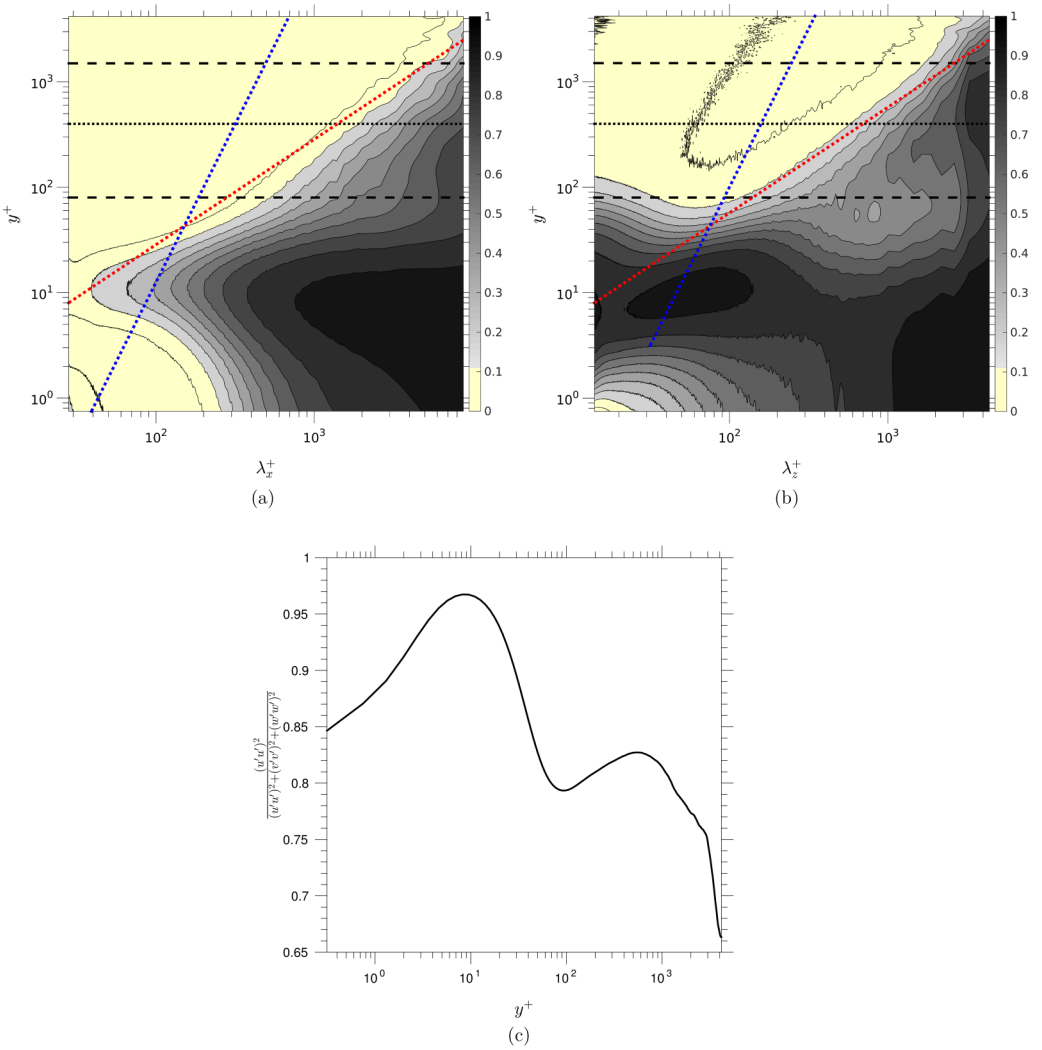

FIG. 4. Characterization of anisotropy due to dominance of streamwise energy $\overline{u'u'}^+ \gg \overline{v'v'}^+, \overline{w'w'}^+$: (a) maps of $(\gamma_u^{1c})^3$ in the streamwise direction, (b) maps of $(\gamma_u^{1c})^3$ in the spanwise direction, and (c) cross-spectrum average of γ_u^{1c}. Red and blue dotted lines are the same as in Fig. 3.

the outer part of the logarithmic layer [31]. Figure 4 also contains a y^+-wise profile of the normalized streamwise energy and this provides confirmation of the existence of energetic structures in the outer layer around $y^+ = 500$. Reference to the $(\gamma_u^{1c})^3$ distribution along the dotted black line at $y^+ = 500$ clearly shows that this peak in streamwise energy is associated with structures having wavelengths of order $\lambda_x^+ \gtrsim 8000$ and $\lambda_z^+ \gtrsim 4000$. The near-wall energy peak at $y^+ \approx 10$ is also clearly brought out in the $(\gamma_u^{1c})^3$ maps, in which a maximum at $\lambda_z^+ \approx 100$ is evidently indicative of the strong small-scale streaks in the buffer layer.

C. Anisotropic range: Small-scale motions

The maps shown in Figs. 3 and 4 contain small-scale ranges to the left of the blue lines $\lambda^+ \propto (y^+)^{1/3}$, which comply with neither isotropy nor one-component dominance. The scales in question are not far from the Kolmogorov range $\lambda^+ \propto (y^+)^{1/4}$. In order to identify the state of the turbulence

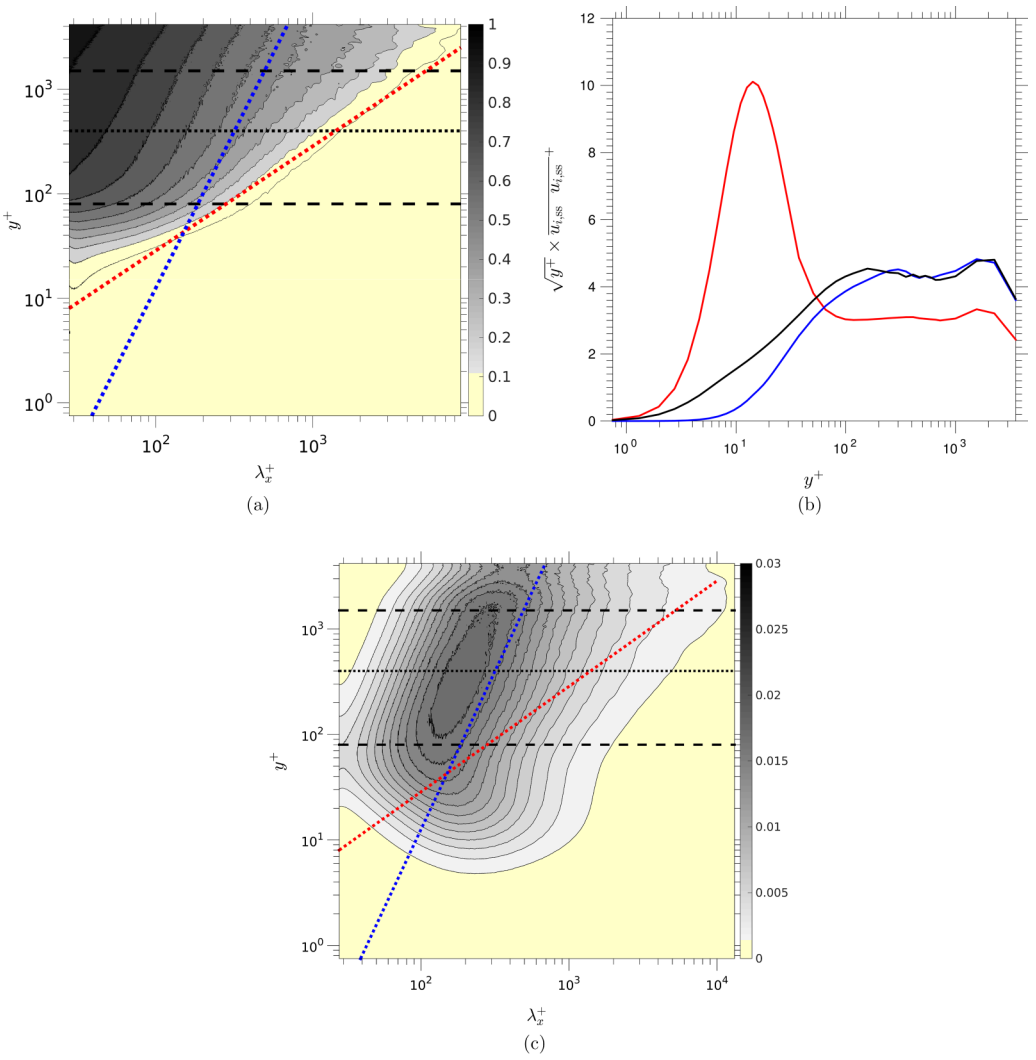

FIG. 5. Characterization of anisotropy of small-scale motions due to dominance of crossflow energy components: (a) map of $(\gamma_{vw}^{2c})^3$, (b) streamwise stress associated with small-scale motions, normalized by $\sqrt{y^+}$ [streamwise stress (red line), wall-normal stress (black line), spanwise stress (blue line)], and (c) compensated power spectra $y\epsilon^{-1/3}k_x^{7/3}\Phi_{uu}$. Red and blue dotted lines are the same as in Fig. 3.

in this range, a third parameter γ_{ij}^{2c} is defined as follows:

$$\gamma_{ij}^{2c} \equiv \frac{2|\Phi_{ii}||\Phi_{jj}|}{|\Phi_{uu}|^2 + |\Phi_{vv}|^2 + |\Phi_{ww}|^2}. \tag{4}$$

This parameter identifies the dominance of two normal components $i \neq j$ over the third and thus highlights the range where the anisotopic turbulence is characteristic of two-component turbulence. Figure 5(a) shows a map of $(\gamma_{vw}^{2c})^3$, which brings into focus the region where the spectra of the wall-normal and spanwise components have similar energy levels, both exceeding the streamwise component. The suggestion emerging from this map is that small-scale motions, of scales λ_x^+ lower than $3.5 \times (y^+)^{1/3}$, are characterized by $\overline{v'_{ss}v'_{ss}}^+ \approx \overline{w'_{ss}w'_{ss}}^+ > \overline{u'_{ss}u'_{ss}}^+$. This rather unexpected result has motivated the isolation of these small scales from larger scales by means of a spatially

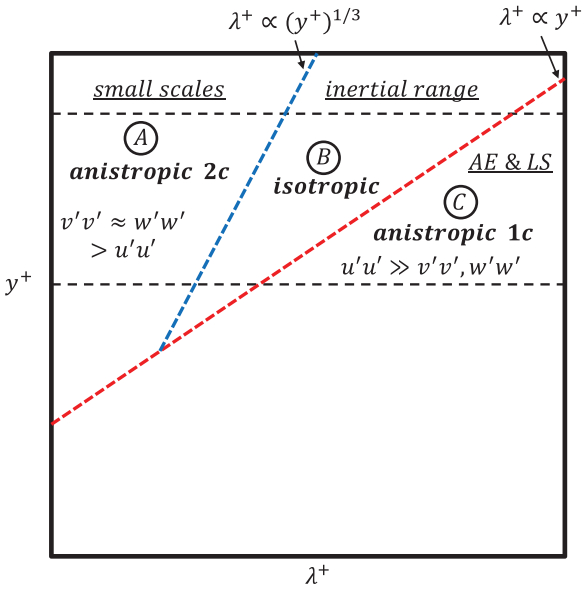

FIG. 6. Subranges in the spectral map having distinct turbulence characteristics (1c: dominance of streamwise component; 2c: dominance of crossflow components; AE: attached eddies; LS: large-scale structures).

two-dimensional version of the empirical mode decomposition, previously used by [32–34]. The distinction between small and large scales is not precise and it depends of the number of intrinsic modes (here 6) used for the separation process. Hence, in the present context, the separation is rather tentative. Nevertheless, the energetic properties of the small scales, shown in Fig. 5(b), support the implication of Fig. 5(a) to the extent that, above the buffer region, the wall-normal and spanwise small-scale energy components exceed the streamwise component. Attention is drawn to the $\sqrt{y^+}$ scaling of the energy components in Fig. 5(b), intended to bring to the fore the constancy of the scaled energy components, the magnitude of which thus varies as $1/\sqrt{y^+}$. The physical significance of the plateau region arising from the $\sqrt{y^+}$ scaling is unclear, at present.

An interesting feature in the small-scale range emerges upon scaling the power spectrum as $y\epsilon^{-1/3}k_x^{7/3}\Phi_{uu}$. The use of k_x scaling reflects the fact that the energy level in the spectrum tends to vary with $k_x^{-7/3}$ in anisotropic turbulence. When the y scaling is added to the compensated spectrum, the resulting map, shown in Fig. 5(c), features an elongated plateau within the mesolayer, just to the left of the blue line $\lambda_x^+ = 3.5 \times (y^+)^{1/3}$. The implication is that the contribution of small-scale energy to the total energy declines inversely with y^+.

D. Summary of subranges

Based on considerations so far, it is possible to identify distinct regions within the spectral map in which the structures possess different characteristics. Such a map is proposed in Fig. 6.

Within the mesolayer, of primary interest herein, there are three major regions.

(1) Region "A", associated with (very) small scales, is characterized by a dominance of the wall-normal and spanwise components over the streamwise fluctuations.

(2) Region "B" is characterized by a trend towards isotropy. This is essentially indicative of the inertial subrange, where the eddies are presumed to be detached.

(3) Region "C" is characterized by a high level of anisotropy in the scales, with the streamwise component dominating and the streamwise and spanwise components larger than the wall-normal component. This region is associated with the attached eddies and with large-scale motion. It is

emphasized here that this region extends across the entire mesolayer. While the associated condition $\Phi_{uu} \propto k^{-1}$ is not clearly present in Fig. 2, an examination of the structure function, to follow, will support the interpretation of this region being associated with attached eddies.

III. ATTACHED-EDDY HYPOTHESIS

A. Structure-function analysis

In the absence of a clear region of $\Phi_{uu} \propto k^{-1}$, conventionally associated with the Townsend-Perry AEH, attention is directed towards the second-order structure function $S_{2,u}(y,\delta)$ as a potentially superior indicator of the validity of the AEH. This is a route previously advocated by Davidson *et al.* [6,7]. Its rationale is based on the observation that there is a close correspondence between the premultiplied spectra and the derivative of the second-order structure function. In particular, Davidson *et al.* argue that, since the two are effectively Fourier-transform pairs, the structure function should exhibit a real-space analog of the k^{-1} spectrum, shown to manifest itself by a constant value of the premultiplied derivative of the structure function. This correspondence is pursued and exploited below.

In channel flow, with homogeneous directions x and z, the relevant second-order structure functions are

$$S_{2,u}(y,\delta_x) = \langle [u(y,x) - u(y,x+\delta_x)]^2 \rangle_{z,t}, \quad S_{2,u}(y,\delta_z) = \langle [u(y,z) - u(y,z+\delta_z)]^2 \rangle_{x,t}, \tag{5}$$

with the subscripts at the end identifying the averaging directions. The structure function essentially represents the total energy contained within the range of eddies with size less than or equal to δ (either δ_x or δ_z). The contribution from eddies larger than δ is negligibly small, because $u(y,x) \approx u(y,x+\delta)$. When $\delta = L$, the largest distance across which there is a correlation between motions at x and $x+\delta$, i.e., with the motions uncorrelated, $S_{2,u}(L)$ reaches a maximum equal to twice the streamwise turbulence energy. At the other extreme, $\delta = 0$, $S_{2,u}(0) = 0$, and the correlation reaches a maximum.

The contribution to the energy associated with eddies having a length δ is given by the premultiplied derivative of the second-order structure function (PMDS2) $\delta \frac{dS_{2,u}(\delta)}{d\delta}$ [1,6]. This is equivalent to, but not the same as, the premultiplied power spectra $(k\Phi_{uu})$. Given a constant level of the PMDS2, which is consistent with a k^{-1} variation of the spectrum [1,6], integration then immediately yields a logarithmic variation of $S_{2,u}(\delta/y)$ and thus a logarithmic dependence $\overline{u'u'}^+(\delta/y)$ for $\delta = L$. In summary then, there is a mutually consistent linkage between a k^{-1} spectrum, a constant level of the PMDS2, the logarithmic variation of $\overline{u'u'}^+$, and the AEH. It is not surprising, therefore, to observe a striking similarity between the premultiplied power spectra and the corresponding PMDS2, as emerges upon comparing the maps in Figs. 7(c) and 7(d) with those in Fig. 2.

Attention is drawn to the fact that the scaling adopted for the abscissa in the x-wise and z-wise maps in Fig. 7 are $8\delta_x$ and $4\delta_z$, respectively. A consequence of including the multipliers 8 and 4, respectively, is that the range of values covered in Fig. 7 corresponds closely to those in Fig. 2. This might seem an arbitrary argument, but there is also some rational justification for it. This emerges upon a closer examination of the relationship between the spectra and the structure function, subject to idealized conditions. Such an examination is presented in the Appendix for two idealized ("toy") conditions. One key relationship that emerges from the considerations in the Appendix is that the spectrum is related to the derivative of $S_{2,u}$ by

$$\frac{dS_{2,u}(\delta)}{d\delta} = 2\frac{d}{d\delta}\left[\int_0^{+\infty} \cos(k_x\delta)\Phi_{uu}(k_x)dk_x\right]. \tag{6}$$

It is this relationship that forms the basis for examining the two toy representations of ϕ_{uu} and the corresponding derivative of the structure function. In particular, monochromatic (with $\lambda = \lambda_{x_0}$) and four-wave-number (with $\lambda_{x_i} < \lambda_{x_0}$, for $i = 1$, 2, and 3) representations of $u(x)$ are examined, and these are argued to imply that the relationship between δ and λ is $\delta = \lambda_{x_0}/4$ for a monochromatic signal, this ratio dropping with increasing number of modes.

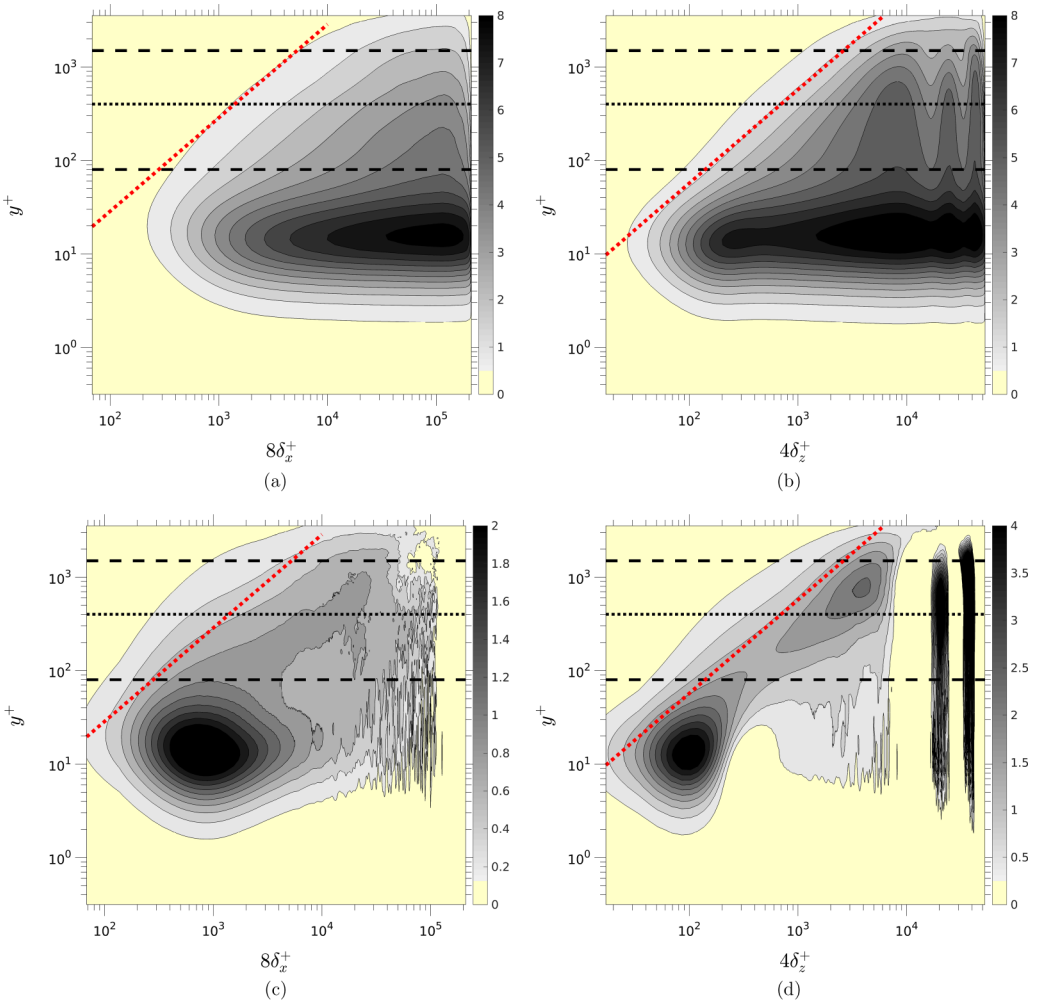

FIG. 7. Maps of the second-order structure function and its premultiplied derivatives: (a) $S_{2,u}(\delta_x)/2$, (b) $S_{2,u}(\delta_z)/2$, (c) $\delta_x(dS_{2,u}/d\delta_x)$, and (d) $\delta_z(dS_{2,u}/d\delta_z)$. Red lines are the same as in Fig. 3.

As is recognized upon comparing Fig. 2(b) with Fig. 7(d), the contours in the PMDS2 matches those in the corresponding premultiplied spectrum if δ_z is multiplied by a factor 4 in the former map. The eddies may thus be associated with a monochromatic signal. In the logarithmic-law region, for $4\delta_z \lesssim 5 \times 10^3$, the wall-normal distribution of the locus of the maximum value follows the relation $\delta_z^+ \propto y^+$, whatever the y locations, the increase towards the maximum value being monotonic. Hence the energy is associated mainly with eddies of a particular size $\delta_{z,o}$, which increase with y. If, in contrast, the coherent structures are described by a range of Fourier modes (with $\lambda \leqslant \lambda_{x_0}$), the qualitative trend is for the ratio $1/4$ to decrease, as demonstrated in the Appendix. In this case, at $\delta = 0$, the curvature of $S_{2,u}(\delta)$ depends of the frequency content of the signal: It strengthens if the signal is associated with a wide range of frequency [1]. This applies to the spectra and structure-function maps in the streamwise direction. Thus, a match between the corresponding maps in the streamwise direction in Figs. 2(a) and 7(c) is obtained if δ_x is multiplied by 8 in the latter map.

The PMDS2 maps conveyed by Figs. 7(c) and 7(d) ($\delta_x dS_{2,u}/d\delta_x$ and $\delta_z dS_{2,u}/d\delta_z$, respectively) show a number of features that are absent or not clearly delineated in the spectra.

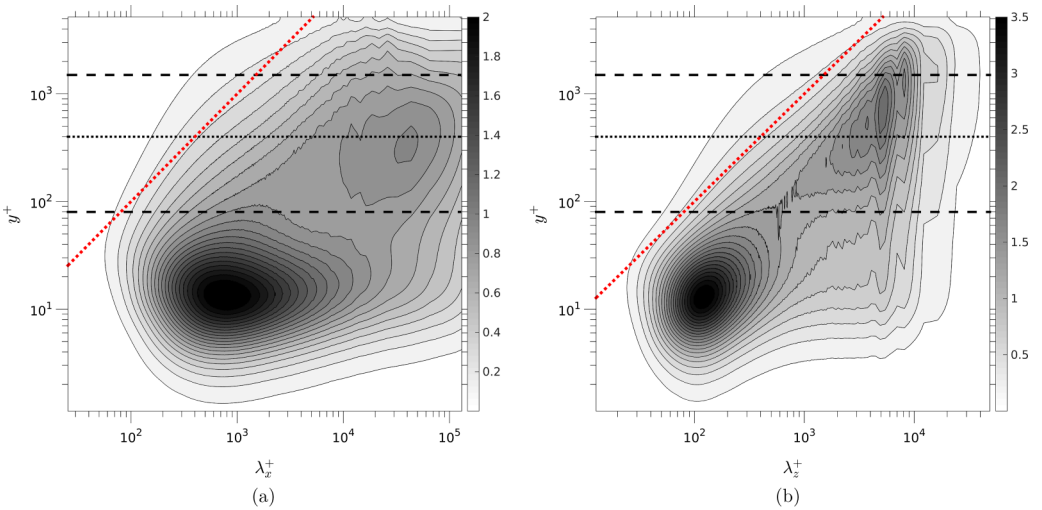

FIG. 8. Premultiplied power spectra of the streamwise fluctuations for $\mathrm{Re}_\tau = 5200$ derived from data by Lee and Moser [28]: (a) streamwise spectra and (b) spanwise spectra.

First, the range of useful resolution in terms of δ_x exceeds that offered in terms of λ_x. This is simply a consequence of tighter limitations on the postprocessing yielding the spectra.

Second, and associated with the first, these figures suggest the presence of spanwise spatial quasiperiodicity in the very large scales, at the extreme right of the map of $S_{2,u}(y,\delta_z)$ [Fig. 7(b)], where an oscillatory pattern at two distinct wavelengths is visible, both also displaying strong wall-normal coherence. These are not captured by the spectra, because of convergence limitations at large wavelengths associated with the relatively small simulation domain. As noted in the Appendix, S_2 is closely associated with the correlation function. Hence, the oscillatory pattern suggests the presence of spanwise-correlated motions. However, in view of the rather small box size (especially πh in the spanwise direction), the question might be posed as to whether the oscillatory behavior seen in Fig. 7(b) and the associated bands in Fig. 7(d) are physically significant.

One part of the answer rests on the observation that the oscillatory behavior arises at $\delta z^+ \approx 5000$ (i.e., $\approx h$) and 10 000, the former value being substantially lower than the spanwise domain size $L_z^+ = 13\,000$. There is reason, therefore, to suppose that at least the shorter-wavelength feature is physically significant, reflecting the spanwise quasiperiodicity of large-scale motions and their footprints, observed by Agostini and Leschziner [32] to be separated by a distance of order h at $\mathrm{Re}_\tau = 1020$.

Support for the above argument is offered by the spectra shown in Fig. 8 for $\mathrm{Re}_\tau = 5200$, obtained from the limited amount of the DNS data available for the large-box simulation of Lee and Moser [28]. The spanwise spectral map is seen to contain spectral bands at $\lambda_z^+ \approx 5000$ and 8000, which support the supposition that the bands in Fig. 7(d) reflect a physical process. There are no such features beyond $\lambda_z^+ \approx 10\,000$.

Third, the seemingly noisy portions present in these maps at low y^+ and intermediate δ values are argued to constitute a physical feature and reflect the fact that medium-scale motions are strongly correlated across the near-wall layer and are present on top of the earlier-mentioned large-scale footprints associated with outer large-scale motions in the upper portion of the mesolayer.

B. Regime of attached eddies

Following Townsend [1] and Davidson *et al.* [6,7], among others, the PMDS2 may be used to shed light on the validity of the AEH. The relevant test is whether $\delta d S_{2,u}/d\delta = \text{const}$ [1,7].

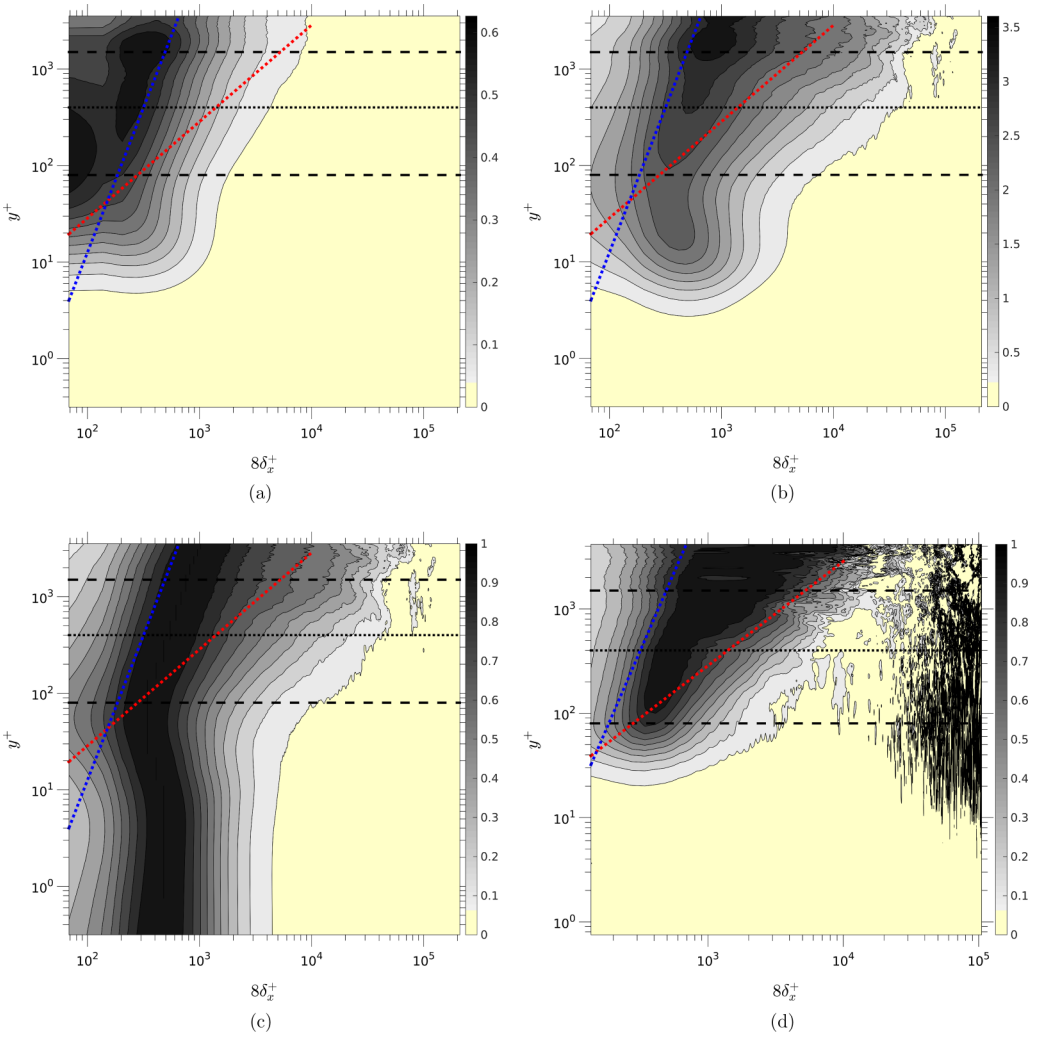

FIG. 9. Turbulence state, premultiplied derivative of the structure function compensated by (a) $\epsilon^{-1/3}\delta_x^{-4/3}$ and (b) $\epsilon^{-2/3}\delta_x^{-2/3}$; (c) the compensated $\delta_x \frac{dS_{2,u}}{d\delta_x}$ defined for the isotropic case is divided by the maximum value at each y location; (d) isotropic parameter $(\gamma^{3c})^2$. Red and blue dotted lines are the same as in Fig. 3.

In Sec. II D it was proposed that the mesolayer may be divided into three physically different domains: A, B, and C in Fig. 6. These are associated, respectively, with spectra of the form $\phi_{uu} \sim \epsilon^{1/3}k_x^{-7/3}$, $\phi_{uu} \sim \epsilon^{2/3}k_x^{-5/3}$, and $\phi_{uu} \sim k_x^{-1}$, the last indicative of the AEH. As argued by Pope [35], a power-law spectrum $\Phi(\omega) \approx C_1\omega^{-p}$ can be related to the second-order structure function $S_p(\delta) \approx C_2\delta^q$, with $p = q + 1$, valid only under the condition that $p > 1$. In accordance with the AEH, $p = 1$, in which case Davidson *et al.* [6,7] show that $S^2(\delta) \approx C_3 \log(\delta) + B$. The implications for subregions A, B, and C in Fig. 6 are, therefore, $\delta_x dS_{2,u}/d\delta_x \sim \epsilon^{1/3}\delta_x^{4/3}$, $\delta_x dS_{2,u}/d\delta_x \sim \epsilon^{2/3}\delta_x^{2/3}$, and $\delta_x dS_{2,u}/d\delta_x = \text{const}$, respectively.

Figure 9(a) shows a map of $\delta_x \frac{dS_{2,u}}{d\delta_x}$ compensated by $\epsilon^{-1/3}\delta_x^{-4/3}$. As expected, on the basis of the above statements on the spectra, there is a plateau in region A, bounded by the blue line. Figure 9(b) relates to the isotropic state through the augmentation by $\epsilon^{-2/3}\delta_x^{-2/3}$, along with a normalized version thereof in Fig. 9(c), in which the levels at any y value are normalized by the maximum at that level.

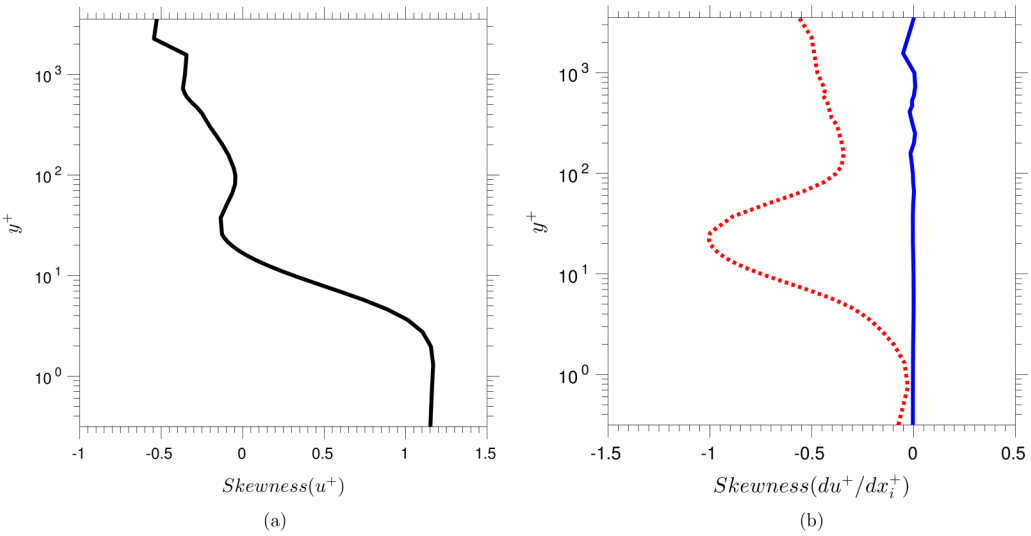

FIG. 10. Wall-normal distribution of (a) the skewness of the streamwise velocity, and (b) the skewness of the streamwise and spanwise derivatives of the streamwise velocity, identified by the red and blue lines, respectively.

Both maps bring to light the plateau in region B in the mesolayer, bounded by the blue and red lines. This region is narrow in the lower part of the layer, but broadens as y increases, i.e., the inertial range becomes wider in the outer portion of the logarithmic layer. These features concur with those in the map in Fig. 4 showing the parameter $(\gamma^{3c})^2$ [see Eq. (2)]. The PMDS2 maps shown in Figs. 7(c) and 7(d), especially the latter, include an oblique band to the right of, and parallel to, the red line, i.e., region C, in which the condition $\delta_x dS_{2,u}/d\delta_x = \text{const}$ is met, at least approximately. Although this provides some support for the validity of the AEH in the mesolayer, the absence of a well-defined plateau is counterindicative. Further support is sought, therefore, from an examination of joint probability density functions (PDFs) pursued below. Implicit in this route being taken is the assumption that the processes in the spectral range C dominates over those in ranges A and B, assumed to make subordinate contributions to cross-scale-averaged PDFs.

In an effort to shed light on any statistical bias in the motions within the mesolayer and thus possibly draw inferences on the shape of the coherent structures, attention is directed first towards the skewness of the PDFs in the mesolayer. Figure 10(a) shows the wall-normal distributions of skewness of the streamwise fluctuations and their streamwise derivative. The inclusion of the latter, in combination with the former, may be argued to allow observations to be made on a streamwise bias in the length scales, which then leads to statements on the shape of the coherent structures. Both figures bring to light a substantial asymmetry in the streamwise fluctuations: few large negative events occurring in combination with many weak positive events. This also suggests asymmetric structural properties of the coherent motions, an issue pursued next by reference to joint PDFs of the streamwise fluctuations and their derivatives.

Figures 11(a) and 11(b) show, respectively, joint $u^+ - du^+/dx^+$ and $u^+ - du^+/dz^+$ PDFs at $y^+ = 600$, a position approximately in the middle of the mesolayer. Conclusions derived for this position apply across the entirely mesolayer, as skewness levels of the PDFs for the velocity fluctuations and their streamwise derivative are fairly uniform. Figure 11(a) reveals four major features: First, consistent with the skewness level in Fig. 10(a), there is a distinct asymmetry in the u^+-fluctuation field; second, weak positive fluctuations occur in combination with high negative du^+/dx^+ values, from which it can be inferred that the length scale of the positive fluctuations is relatively small; third, strong negative fluctuations occur in combination with low values of positive

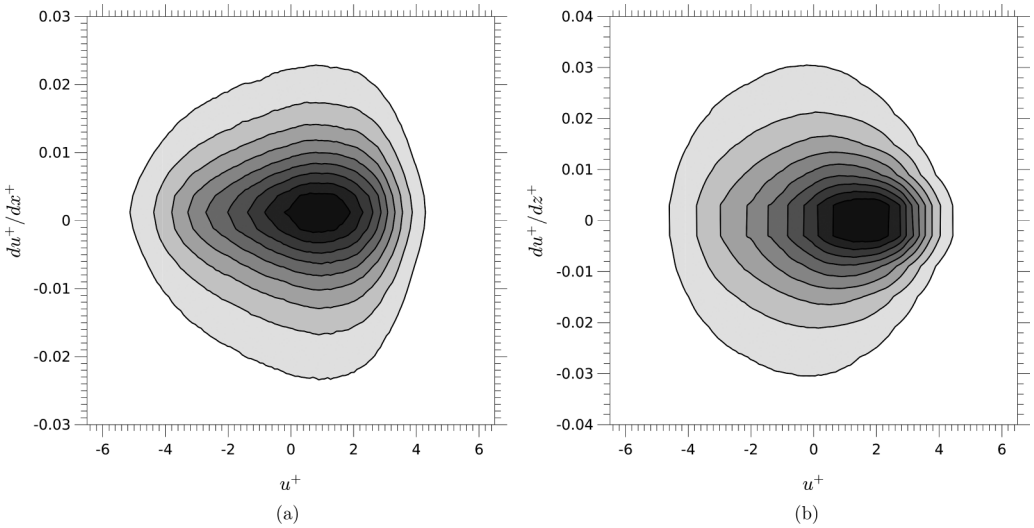

FIG. 11. Joint PDFs between the streamwise velocity and its derivative at $y^+ \approx 600$: (a) $u^+ - du^+/dx^+$ and (b) $u^+ - du^+/dz^+$. The PDF contours identify 0.1–0.9 of the PDF height at constant increment 0.1, subject to total PDF volume normalized to 1.

du^+/dx^+, suggesting relatively large length scales; fourth, negative values of du^+/dx^+ tend to be larger than positive ones, in line with the skewness level in Fig. 10(b). There is therefore a bias in the length scales associated with deceleration and acceleration, with the latter less numerous, but more intense. In Fig. 11(b) it is observed, first, that the contours of du^+/dz^+ are symmetric. This concurs with the zero-skewness line of the PDFs of du^+/dz^+ in Fig. 10(b). Second, and in contrast to the PDF in Fig. 11(a), large spanwise gradients occur in combination with negative u^+ fluctuations, while low spanwise gradients occur in combination with high-velocity fluctuations. Again, through interpretation of these combinations as conveying information on the length scale, it may be inferred that the spanwise length scale is relatively large in combination with positive fluctuations and relatively small in combination with negative fluctuations.

The skewness distributions, and the length scales inferred, qualitatively, from the joint PDFs in Fig. 11 and the ratio between λ and δ previously argued, suggest the form of coherent structures conveyed conceptually in Fig. 12. This structure, symmetric in the spanwise direction and tail-like in the streamwise direction, arguably provides support for the AEH. In particular, it is consistent with the sequence of several generations of attached eddies, as indicated in the sketch.

Further evidence in support of the AEH is provided by features contained in the maps of the PMDS2 in Figs. 7(c) and 7(d). These maps are reproduced in Figs. 13 and 14, in which two regions are highlighted: a blue triangular region and a more restricted red trapezoidal region, both covering the mesolayer.

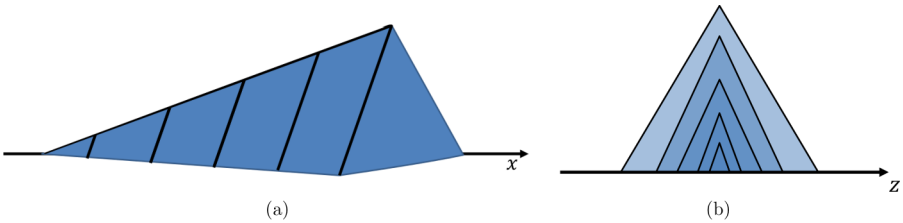

FIG. 12. Conceptual sketch of the 'shape' of the coherent structures associated with attached eddies.

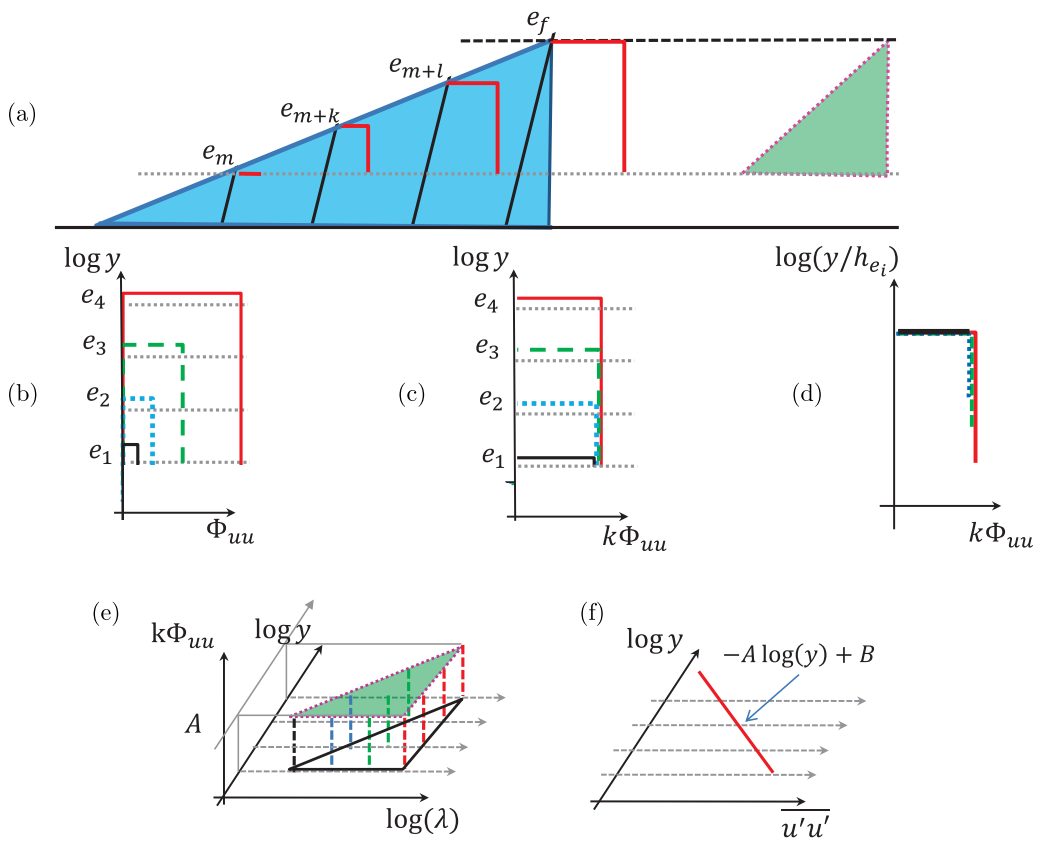

FIG. 13. Conceptual representation of the conventional attached-eddy hypothesis pertaining to a triangular plateau region in the spectrum or PMDS2 map: (a) and (b) hierarchy of attached eddies e_m, e_{m+k}, etc., (c) eddy energy density normalized by λ, (d) eddy size normalized by h_{e_i}, (e) normalized eddies in the triangular plateau region, and (f) resulting logarithmic profile of streamwise turbulence energy.

If a perfect plateau in the PMDS2 and the corresponding premultiplied spectra existed within the triangular region, the implications regarding the AEH would be those shown in the schematic in Fig. 13. In this conceptual representation, e_i are representative attached eddies. Notional y-wise variations of the eddies' respective energy contributions $\overline{u'u'}^+$ and scaled variations thereof, with the scaling variables being the eddy height h and wavelength λ, are shown alongside the conceptual attached-eddy sketch. The collapse in the scaled uniform profiles reflects the linear dependence of the eddy height on y and the implied constancy of $k\Phi_{uu}$ in the premultiplied spectra. This is then fully consonant with the AEH and also with logarithmic variation of $\overline{u'u'}^+$ expressed by Eq. (1).

As is evident from Fig. 7, there is no clear plateau within the triangular region, probably because the Reynolds number is low. However, there is an approximately constant level within the red trapezoidal region. One consequence of this restricted plateau region is that the logarithmic variation in Eq. (1) only applies in the upper portion of the mesolayer, above the dotted line in Figs. 7(c) and 7(d). Below that line, the linear variation of the parallel boundaries of the trapezoid, when transcribed to the premultiplied spectra, implies a constant level of $\overline{u'u'}^+$, broadly in line with the variations shown in Fig. 1.

The restricted plateau region in the trapezoidal region leads to the interpretation shown in Fig. 14. Prior to this interpretation, however, Fig. 13 provides the conventional view introduced by Townsend, as a background against which to discuss Fig. 14.

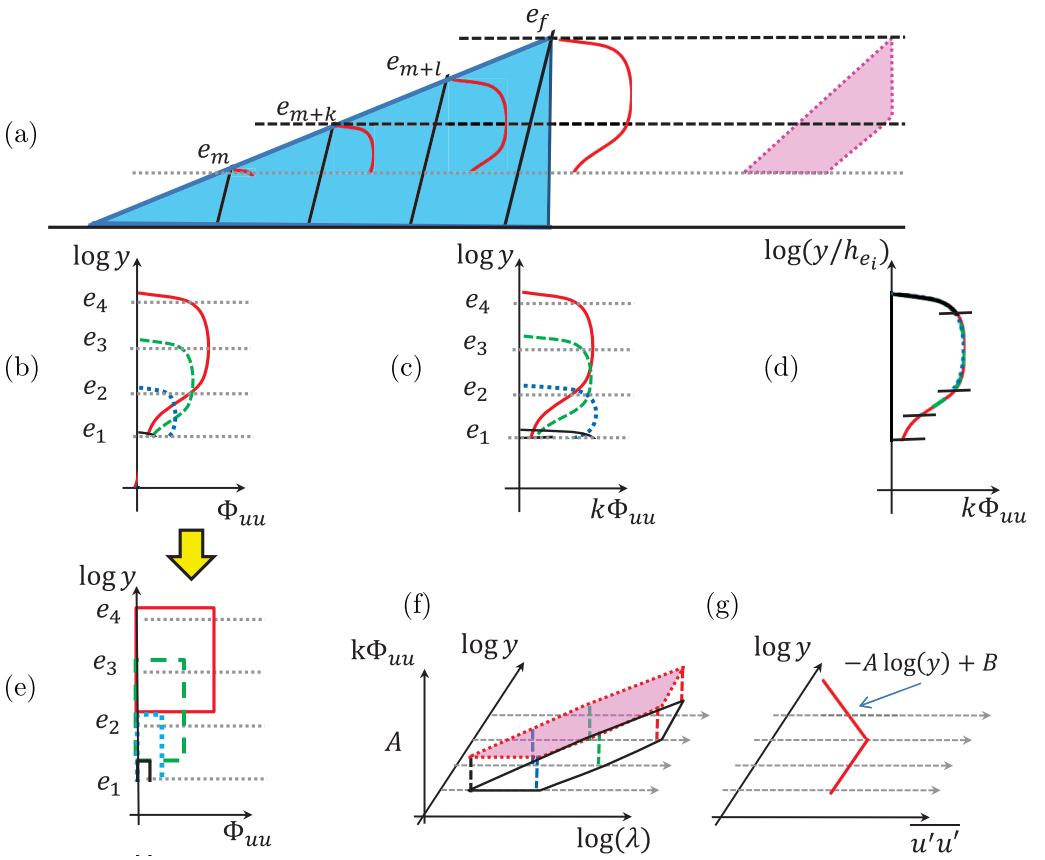

FIG. 14. Conceptual representation of the modified attached-eddy hypothesis pertaining to the trapezoidal plateau region in the spectrum or PMDS2 map: (a) and (b) hierarchy of attached eddies e_m, e_{m+k}, etc., (c) eddy energy density normalized by λ, (d) eddy size normalized by h_{e_i}, (e) idealized representation of the energy density profiles sketched in (b), (f) normalized eddies in the trapezoidal plateau region, and (g) resulting logarithmic and constant portions in profile of streamwise turbulence energy.

The sketches in Figs. 13(b)–13(d) show a sequence of four attached eddies e_1–e_4, whose energy rises with height such that the eddies collapse if the energy density and height are normalized by $\lambda = 1/k = y$, i.e., the eddies are self-similar. If these eddies exist in the triangular region of the spectrum, within which $k\Phi_{uu} = \text{const} = A$, limited between $\lambda_{\min} = y$ and $\lambda_{\max} = \text{const}$, as shown in Fig. 13(e), it follows that the energy $\overline{u'u'}$ varies logarithmically with y, as shown in Fig. 13(f), which arises from Eq. (1). The implication is thus that, at any y location, only eddies larger than the attached eddy at that height contribute to the energy and that all such eddies contribute at the level $k\Phi_{uu} = A$.

Figure 14 now pertains to the trapezoidal domain shown in Fig. 7. The upper part of this domain is triangular, which thus conforms to the relationship shown in Fig. 13. Figures 14(b)–14(e) relate to the parallelogram below the triangular region, with Fig. 14(e) being an idealized representation of the profiles in Fig. 14(b). As before, the normalization $k\Phi_{uu} = A$ applies, but only over a restricted height of the eddies. Below the height defined by the lower line of the parallelogram $\lambda_{\max}(y)$, the energy of the eddy declines rapidly (notionally) in a step-change manner to zero, as indicated by the transition between the two sketches in Figs. 14(b) and 14(e). If next $\overline{u'u'}(y)$ is evaluated by integration between the parallel lines $\lambda_{\min}(y)$ and $\lambda_{\max}(y)$, the lines bounding the parallelogram [see Fig. 14(f)], the result is a plateau of $\overline{u'u'}$, as shown in Fig. 14(g).

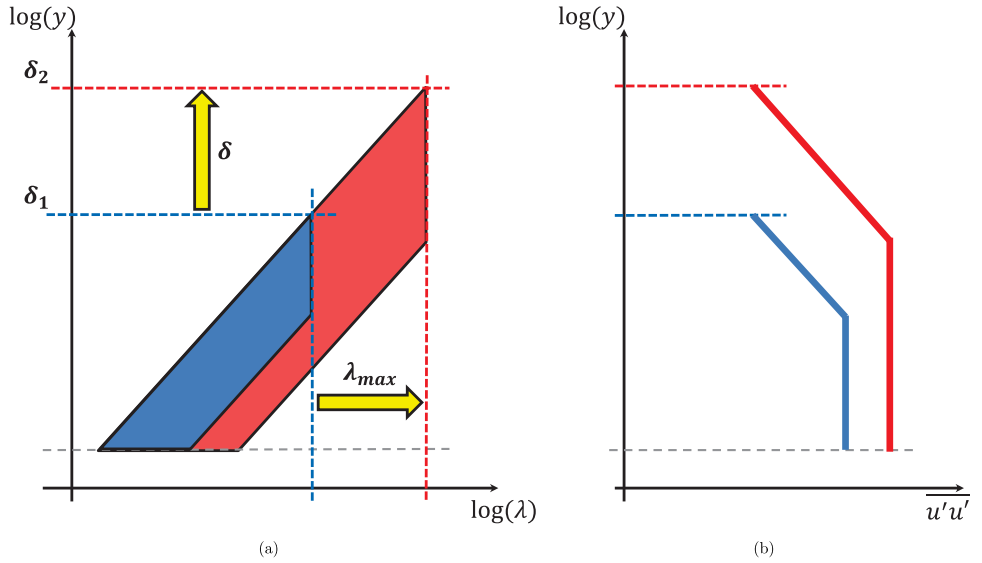

FIG. 15. Conceptual representation of the consequences of increasing Reynolds number: (a) enlargement of trapezoidal plateau region, and (b) increase in the streamwise-energy plateau and wall-normal extension of the logarithmic region.

This representation differs substantially from the conventional AEH, but does imply a self-similar set when scaling with h and λ is effected. It is thus arguable that the plateau region within the trapezoidal region in Figs. 7(c) and 7(d) is fundamentally consistent with the AEH even though there is no clearly defined triangular plateau region. This interpretation also explains the plateau in the $\overline{u'u'}$ profile.

As an aside, although relevant to the above argument, it is interesting to consider the consequence of the Reynolds number being increased. On the assumption that the trapezoidal area is maintained, the change with the Reynolds number leads to the blue region in Fig. 15 changing to the red area, subject to $\lambda_{\min}(y)$ remaining invariant. The consequence is then an increase in the plateau of $\overline{u'u'}$ and an extension of the logarithmic decline in $\overline{u'u'}$, as observed by Smits *et al.* [27], Hultmark *et al.* [14,25], and Vallikivi *et al.* [36], among others.

Observations that give added support to the above arguments linking the AEH to the trapezoidal plateau region arise from averaging over a restricted segment of the DNS data, following the transient phase and covering approximately two global eddy-turnover periods within the interval $2800 \leqslant t^+ \leqslant 3150$. It is emphasized here that this is done merely in order to add support to the validity of the relationship between the plateau in the trapezoidal area in Fig. 14 and the logarithmic decline of $\overline{u'u'}^+(y^+)$ in the mesolayer. The principal consequence of this restricted averaging is that the influence of the large-scale motion in the outer part of the logarithmic layer on the statistics is reduced relative to averaging over the full duration of the simulation; the outer large-scale motions are observed to strengthen over the simulation period.

Maps of PMDS2 for the restricted interval are shown in Figs. 16(a) and 16(b), while the variation of the related streamwise-energy component is shown in Fig. 17. Upon comparing these maps in Figs. 7(c) and 7(d), it is immediately apparent that the nearly constant level within the trapezoidal area, the plateau region, is far more pronounced in the former than in the latter. This is accentuated by the δ_x- and δ_z-wise profiles of the PMDS2, at different y^+ levels within the mesolayer, shown in Figs. 16(c) and 16(d), respectively. The profiles in the latter plot, in particular, feature a nearly constant level across the diagonal band contained within the trapezoidal region in Fig. 14. Based on the previously discussed relationships between the spectra, the PMDS2, and the logarithmic

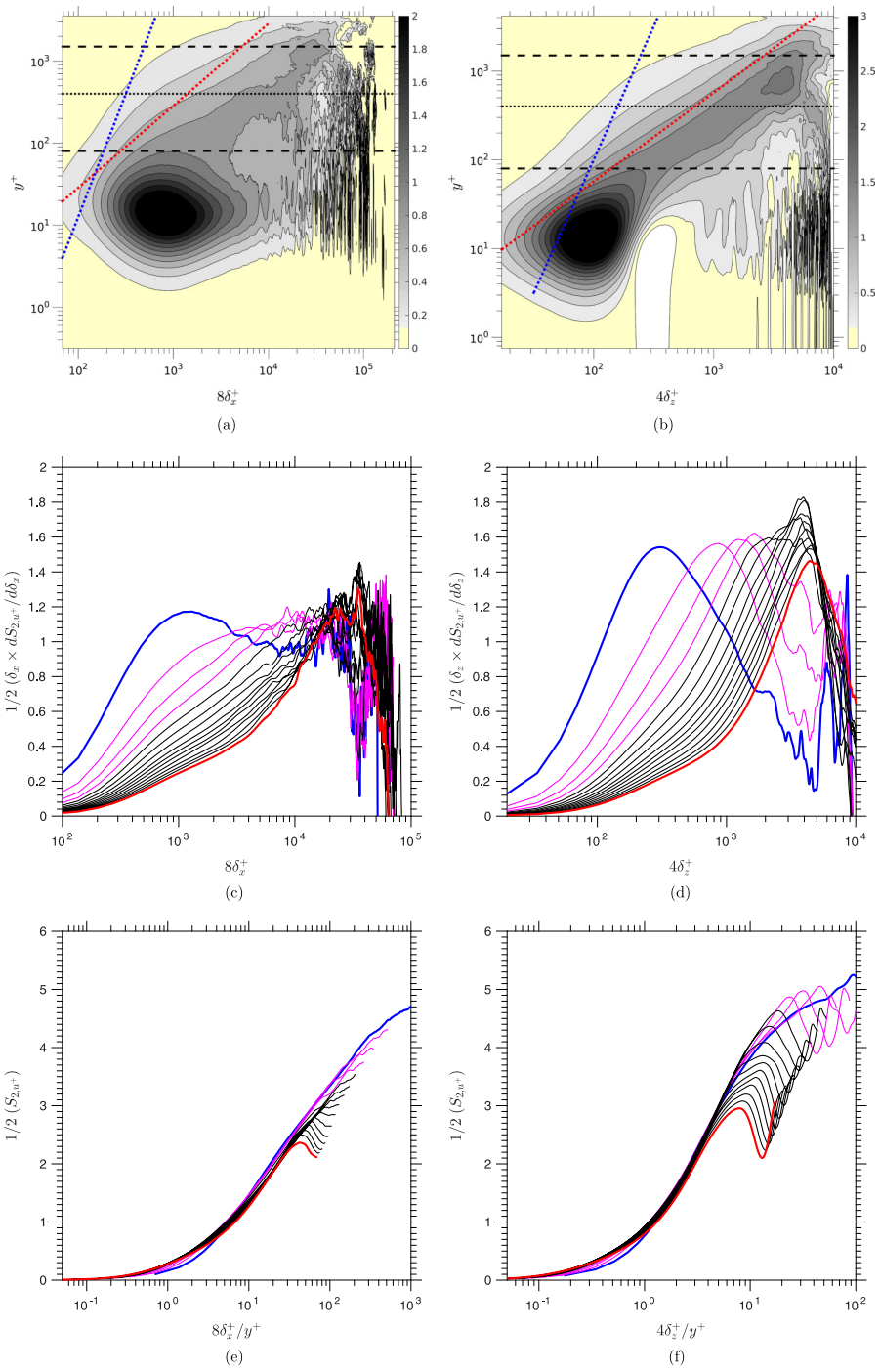

FIG. 16. Statistics for the restricted interval $2800 \leqslant t^+ \leqslant 3150$: (a) and (b) maps of PMDS2 in the streamwise and spanwise directions, respectively; (c) and (d) profiles of PMDS2 as functions of streamwise and spanwise wavelengths, respectively, starting from $y^+ = 100$ (blue line) up to $y^+ = 1200$ (red line) in increments of 100; and (e) and (f) profiles of $S_{2,u}$ as functions of streamwise and spanwise wavelengths, respectively, starting from $y^+ = 100$ (blue line) up to $y^+ = 1200$ (red line) in increments of 100.

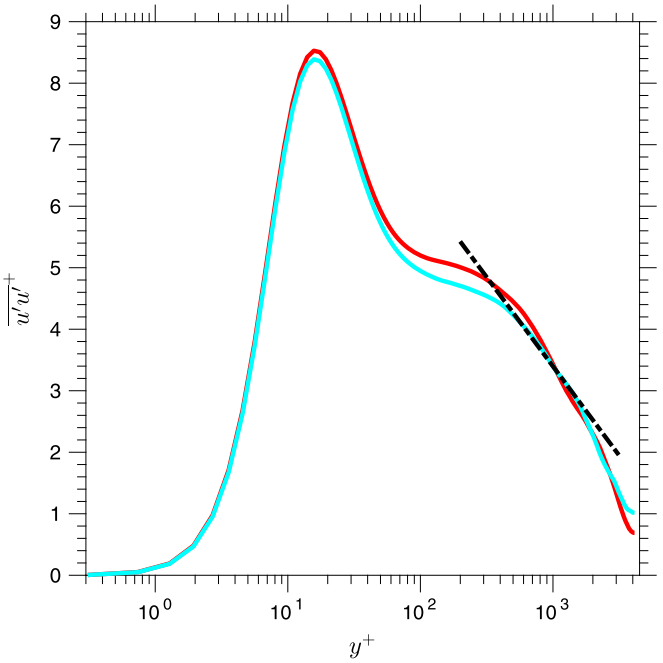

FIG. 17. Wall-normal distribution of the streamwise stress for the restricted interval: $2800 \leqslant t^+ \leqslant 3150$ (cyan line) and $4200 \leqslant t^+ \leqslant 4900$ (red line). The profile derived from the full simulation period is given in Fig. 1. The dashed line represents the variation $\overline{u'u'}^+ = -1.26 \log y^+ + 12.2$.

law in Fig. 17, the expectation is that the levels of both plateau regions in Figs. 16(c) and 16(d) would be 1.26. This value is reasonably well returned in the streamwise-scale map, but is higher in the spanwise-scale map. It is noteworthy that the differences between the two PMDS2 maps are mirrored by similar differences in the spectra at both $\mathrm{Re}_\tau = 4200$ and 5200. While the origin of the difference is difficult to identify unambiguously, an issue that may play a role is that the spanwise eddy scales are constrained relative to the streamwise scales by the presence of wall-normal confinement. This is in contrast to unconfined boundary layers. As eddies evolve, wall-normal growth is inhibited and energy is accumulating in eddies whose spanwise separation has to scale with h. This is not the case, however, with respect to streamwise scales, which can grow without inhibition.

Figures 16(e) and 16(f) confirm two observations made previously by Davidson *et al.* [6,7], albeit only with respect to the streamwise scales and for a much narrower range of y^+. First, at any y^+, the increase in the structure function with δ^+ is logarithmic; second, the profiles collapse reasonably well when δ is scaled with y^+. This behavior is again compatible with the AEH.

Consistent with the above features, the logarithmic decay of $\overline{u'u'}^+$ in the upper portion of the mesolayer $400 < y^+ < 1200$, shown in Fig. 17, is considerably more pronounced than in the corresponding profile in Fig. 1. In this range, $\overline{u'u'}^+$ follows $A \log y^+ + B$ with $A = 1.26$ and $B = 12.2$. Based on the AEH, Perry *et al.* [3] show that the constant A must be universal and that B depends of the large-scale motions. As shown by Hultmark *et al.* [25], Marusic *et al.* [13], Vallikivi *et al.* [36], and Chung *et al.* [9], in pipe flow and turbulent boundary layers, the value of the Townsend-Perry constant A lies in the interval 1.24–1.26.

A final observation made here on the PMDS2 map in Fig. 16(b) relates to the presence of four fingers in the sublayer, emanating from the region above it. These appear to be footprints of

structures present in the mesolayer. Remarkably, they are equidistant in logarithmic units, indicating a sequential doubling in the eddy size, which is in agreement with the paradigm of Perry *et al.*

IV. SUMMARY AND CONCLUSIONS

The availability of DNS data for channel flow at the credibly high-friction Reynolds number of 4200 has provided a rewarding foundation for exploring open questions on structural and spectral properties of near-wall turbulence. The examination has been undertaken by reference to maps of properties in the spectral–wall-normal space, the former being either the wavelength, in the case of spectra, or the separation distance, in the case of the structure function. The first objective has been to examine the properties of turbulence across the spectral range from small-scale motions to the largest resolved motions. To this end, different anisotropy parameters were defined, and maps of these parameters were examined, alongside premultiplied and compensated spectra and the premultiplied derivative of the second-order structure function, the latter shown to be closely related to the former. Primary emphasis was put on the mesolayer essentially, the logarithmic-law layer spanning the range $80 < y^+ < 2000$.

The first important result derived from the above is a map in wall-normal-distance–wavelength space in which three major subranges were identified within the mesolayer: (A) a subrange at short wavelength (small-scale eddies) in which turbulence is anisotropic, characterized by a dominance of wall-normal and spanwise energy components over the streamwise component and the spectrum $\Phi_{uu} \propto k_x^{-7/3}$; (B) a central range, which conforms to the conventional view of close to isotropic turbulence in which $\Phi_{uu} \propto k_x^{-5/3}$; and (C) a subrange at long wavelength in which the streamwise-energy component dominates and in which the spectrum complies with a variation not far from $\Phi_{uu} \propto k^{-1}$. The first result (A) is rather counterintuitive, as the expectation is that turbulence in the smallest range of eddies should be close to isotropic. Importantly, the subrange (C) is not merely confined to the longest wavelength, but extends, in lower parts of the logarithmic-law mesolayer, well into the range of low wavelengths.

The above investigation, and its results, formed the background against which the second major objective was pursued, namely, to examine whether the attached-eddy hypothesis is valid within the mesolayer. To this end, attention focused primarily on the premultiplied derivative of the second-order structure function, in preference to the premultiplied spectrum. This preference is based on the observation that the two are closely related, while the latter is a more promising foundation for examining the validity of the AEH, in particular, because the latter brings to light, much more clearly than the former, the telltale plateau region with which the AEH is associated. This examination was further aided by the inclusion of one-dimensional PDFs for the streamwise-velocity fluctuations and their streamwise derivative, both displaying significant levels of negative skewness in the mesolayer and of joint PDFs between the streamwise fluctuations and their streamwise or spanwise derivatives.

A conclusion derived from the PDFs is that the coherent structures in the mesolayer feature a shape that is characterized by a broad and short head and a narrow long tail, consistent with existence of a hierarchical structure of attached eddies. Consideration of the PMDS2 in wall-normal–spanwise-separation space brought to light a trapezoidal region, contained with the subregion (C) in the wall-normal–wavelength map, in which the PMDS2 level is close to being constant. Based on conceptual arguments, closely connected to the conventional concept of self-similarity of the scaled energy of attached eddies in a triangular plateau region, the present observations of an approximate plateau in the trapezoidal region led to the conclusion that self-similarity, and hence the AEH, also applies across the entire mesolayer. An interesting implication of the trapezoidal shape, when assumed transcribable to the spectral map, is that the upper part of the mesolayer is consistent with a logarithmic decay of the streamwise energy, while the lower part of the mesolayer is consistent with a constant level of energy, a behavior broadly consistent with the directly computed (or measured) y-wise profile of the streamwise energy.

ACKNOWLEDGMENTS

We are grateful to Dr. Lozano-Durán and Professor Jiménez for making available their DNS database, which formed the basis of the analysis in this paper. We would also like to thank Dr. Lee and Professor Moser for allowing us to use data derived from their channel-flow DNS for $\mathrm{Re}_\tau = 5200$.

APPENDIX: RELATIONSHIP BETWEEN THE SPECTRA AND THE STRUCTURE FUNCTION

First, as noted earlier, $S_{2,u}(\delta)$ may be related to the correlation between the turbulent motions δ apart. If the covariance is defined as $\mathrm{cov}(\delta) = 2\int_0^{+\infty} \Phi_{ii}(\omega)\cos(\omega\delta)d\omega$, where $\omega = 2\pi k_x$ (or $\omega = 2\pi k_z$), the dependence on the correlation function arises from

$$\begin{aligned} S_{2,u}(\delta) &= \langle [u(y,x) - u(y,x+\delta)]^2 \rangle \\ &= \langle u(y,x)^2 \rangle + \langle u(y,x+\delta)^2 \rangle - 2\langle u(y,x)u(y,x+\delta) \rangle \\ &= 2[\mathrm{cov}(0) - \mathrm{cov}(\delta)] \\ &= 2\overline{u'u'}[1 - F_u(\delta)], \end{aligned} \tag{A1}$$

$$\frac{dS_{2,u}(\delta)}{d\delta} = -2\overline{u'u'}\frac{dF_u(\delta)}{d\delta}. \tag{A2}$$

The variation of the correlation function, from its lower limit $F_u(0) = 1$, is monotonic if the signal contained a wide range of eddy sizes (as in turbulent flow); the expectation is that the upper limit is $F_u(L \to \infty) = 0$. For example, $F_u(\delta)$ may be oscillatory if there are quasiregular coherent packets of motion within the range of δ being considered. In the spanwise direction, the second-order structure function and its derivative, conveyed by Figs. 7(b) and 7(d), respectively, brings into focus that the large-scale structures ($\lambda_z \approx 5 \times 10^3$) are strongly coherent in the spanwise direction, unlike those in the streamwise direction where no oscillatory behavior is identifiable in the contour maps shown in Figs. 7(a) and 7(c).

Next, the one-dimensional spectrum can be related to the correlation function via the Fourier transform

$$\Phi_{uu}(k_x) = \frac{2}{\pi}\int_0^{+\infty} F_{u_i}(\delta)\cos(k_x\delta)d\delta. \tag{A3}$$

Using Eqs. (A1) and (A3) and the covariance definition given earlier, the following relationship can be derived between the spectra and the structure function:

$$\begin{aligned} S_{2,u_i}(\delta) &= 2\left[\int_0^{+\infty} \Phi_{uu}(k_x)dk_x - \int_0^{+\infty} \Phi_{uu}(k_x)\cos(k_x\delta)dk_x\right] \\ &= 2\int_0^{+\infty} [1 - \cos(k_x\delta)]\Phi_{uu}(k_x)dk_x. \end{aligned} \tag{A4}$$

Consequently, the energy density is related to the derivative of S_{2,u_i} by

$$\frac{dS_{2,u}(\delta)}{d\delta} = 2\frac{d}{d\delta}\left[\int_0^{+\infty} [\cos(k_x\delta)]\Phi_{uu}(k_x)dk_x\right]. \tag{A5}$$

The equivalence between δ and $\lambda_x(=2\pi/k_x)$ is explored here by reference to toy signals of the form

$$u(x) = \sum_{n=1}^{N} \frac{A}{nk_0}\sin(nk_0x + \pi), \tag{A6}$$

with $N = 1$ or 4. Figure 18(a) shows distributions of $u(x)$, the associated spectra, the structure function, and its derivative for both cases. For $N = 4$, attention is drawn to the fact that the amplitude

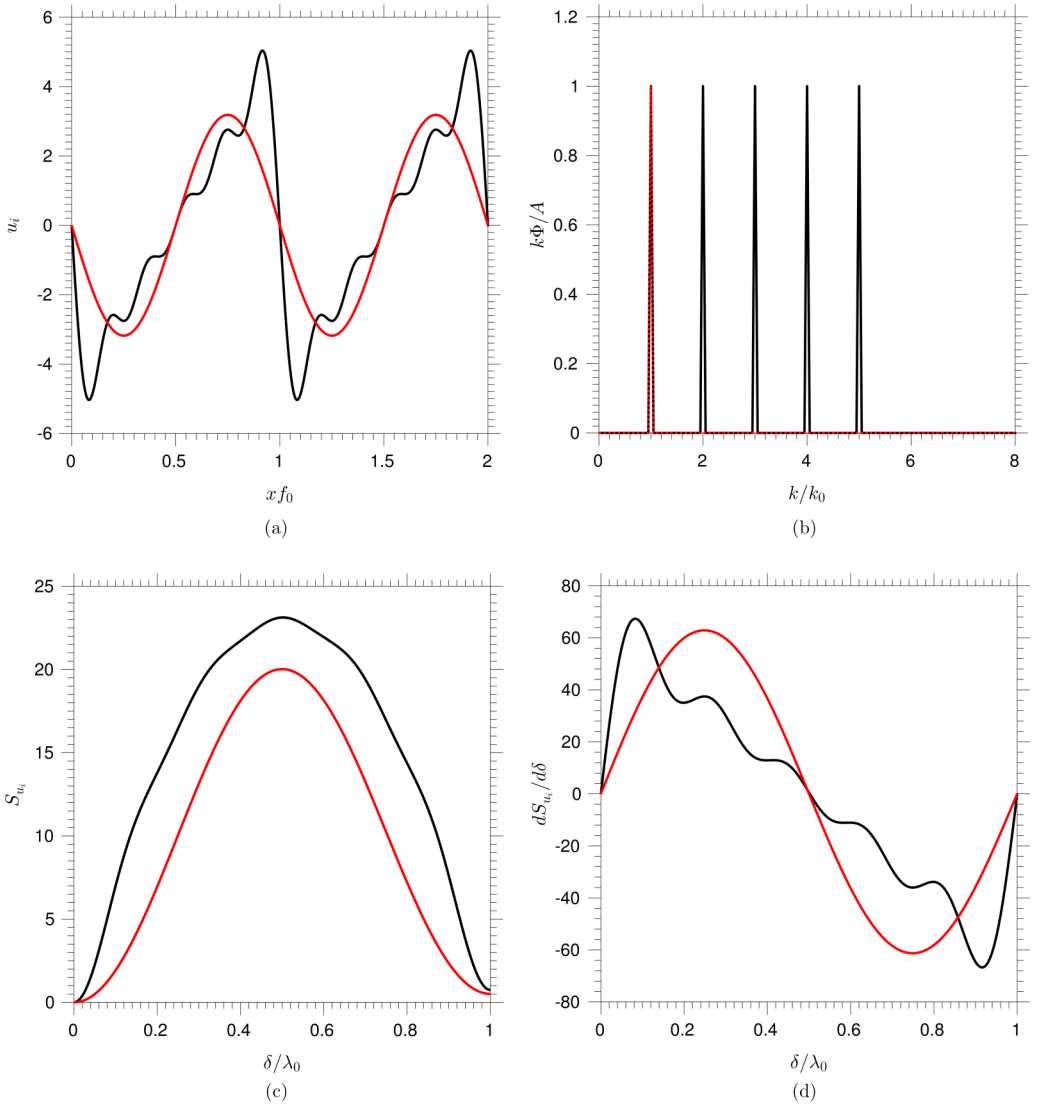

FIG. 18. Toy problems illustrating the relationship between spectra and structure function: (a) signals determined from Eq. (A6) with $N = 1$ and $N = 4$, identified by the red and black lines, respectively, (b) the premultiplied power spectrum for both signals, (c) the second-order structure function, and (d) the derivative of the structure function.

associated with each mode decreases as the frequency increases, such that $k_i\Phi_i = \text{const}$ $(i = 1, N)$, as conveyed by the premultiplied power spectra, which may be interpreted as a discrete version of the AEH.

For $N = 1$, $u(x) = A\cos(k_{x_0}x + \varphi)$, it follows that $\Phi_{uu} = A^2\delta_d(k_{x_i} - k_{x_0})$, with δ_d being the Dirac function, and Eq. (6) then gives

$$\frac{dS_{2,u}(\delta)}{d\delta} = \frac{d}{d\delta}\left[A^2\cos\left(k_{x_0}\delta\right)\right] = A^2k_{x_0}\sin\left(k_{x_0}\delta\right). \tag{A7}$$

This derivative reaches a maximum for $k_{x_0}\delta = \frac{\pi}{2}$, i.e., $\delta = \lambda_{x_0}/4$, as can be seen in Fig. 18(d).

When the 'coherent' structures arise from several smaller eddies with lower energy, the increase of the $S_{2,u}$ is sharper than in the monochromatic case, with a slope variation associated with the effect of different-sized eddies. The maximum of the derivative of $dS_{2,u_i}/d\delta$ is observed to shift to the left and this implies a decreasing ratio δ/λ. While the actual value clearly depends on the number of modes (or eddies) and is thus uncertain in real turbulence, it is a fact that the coherent structures are composed of a range of eddies and this necessarily results in a ratio between δ and λ lower than that for the monochromatic case.

[1] A. A. Townsend, *The Structure of Turbulent Shear Flow* (Cambridge University Press, Cambridge, 1980).

[2] A. Perry and M. Chong, On the mechanism of wall turbulence, J. Fluid Mech. **119**, 173 (1982).

[3] A. Perry, S. Henbest, and M. Chong, A theoretical and experimental study of wall turbulence, J. Fluid Mech. **165**, 163 (1986).

[4] A. Perry and I. Marusic, A wall-wake model for the turbulence structure of boundary layers. Part 1. Extension of the attached eddy hypothesis, J. Fluid Mech. **298**, 361 (1995).

[5] T. B. Nickels, I. Marusic, S. Hafez, and M. S. Chong, Evidence of the k_1^{-1} Law in a High-Reynolds-Number Turbulent Boundary Layer, Phys. Rev. Lett. **95**, 074501 (2005).

[6] P. A. Davidson, T. B. Nickels, and P.-Å. Krogstad, The logarithmic structure function law in wall-layer turbulence, J. Fluid Mech. **550**, 51 (2006).

[7] P. A. Davidson, P.-Å. Krogstad, and T. B. Nickels, A refined interpretation of the logarithmic structure function law in wall layer turbulence, Phys. Fluids **18**, 065112 (2006).

[8] C. de Silva, I. Marusic, J. Woodcock, and C. Meneveau, Scaling of second-and higher-order structure functions in turbulent boundary layers, J. Fluid Mech. **769**, 654 (2015).

[9] D. Chung, I. Marusic, J. Monty, M. Vallikivi, and A. Smits, On the universality of inertial energy in the log layer of turbulent boundary layer and pipe flows, Exp. Fluids **56**, 110 (2015).

[10] J. D. Woodcock and I. Marusic, The statistical behavior of attached eddies, Phys. Fluids **27**, 015104 (2015).

[11] Y. Hwang, Statistical structure of self-sustaining attached eddies in turbulent channel flow, J. Fluid Mech. **767**, 254 (2015).

[12] J. Jiménez and S. Hoyas, Turbulent fluctuations above the buffer layer of wall-bounded flows, J. Fluid Mech. **611**, 215 (2008).

[13] I. Marusic, J. P. Monty, M. Hultmark, and A. J. Smits, On the logarithmic region in wall turbulence, J. Fluid Mech. **716**, R3 (2013).

[14] M. Hultmark, M. Vallikivi, S. Bailey, and A. Smits, Logarithmic scaling of turbulence in smooth-and rough-wall pipe flow, J. Fluid Mech. **728**, 376 (2013).

[15] B. Rosenberg, M. Hultmark, M. Vallikivi, S. Bailey, and A. Smits, Turbulence spectra in smooth-and rough-wall pipe flow at extreme Reynolds numbers, J. Fluid Mech. **731**, 46 (2013).

[16] A. Lozano-Durán and J. Jiménez, Effect of the computational domain on direct simulations of turbulent channels up to $\mathrm{Re}_\tau = 4200$, Phys. Fluids **26**, 011702 (2014).

[17] A. Lozano-Durán and J. Jiménez, Time-resolved evolution of coherent structures in turbulent channels: Characterization of eddies and cascades, J. Fluid Mech. **759**, 432 (2014).

[18] K. C. Kim and R. J. Adrian, Very large-scale motion in the outer layer, Phys. Fluids **11**, 417 (1999).

[19] J. Del Álamo and J. Jiménez, Spectra of the very large anisotropic scales in turbulent channels, Phys. Fluids **15**, L41 (2003).

[20] N. Hutchins and I. Marusic, Evidence of very long meandering features in the logarithmic region of turbulent boundary layers, J. Fluid Mech. **579**, 1 (2007).

[21] I. Marusic, R. Mathis, and N. Hutchins, High Reynolds number effects in wall turbulence, Int. J. Heat Fluid Flow **31**, 418 (2010).

[22] R. Mathis, N. Hutchins, and I. Marusic, Large-scale amplitude modulation of the small-scale structures in turbulent boundary layers, J. Fluid Mech. **628**, 311 (2009).

[23] J. Vassilicos, J.-P. Laval, J.-M. Foucaut, and M. Stanislas, The streamwise turbulence intensity in the intermediate layer of turbulent pipe flow, J. Fluid Mech. **774**, 324 (2015).
[24] N. Hutchins, T. B. Nickels, I. Marusic, and M. Chong, Hot-wire spatial resolution issues in wall-bounded turbulence, J. Fluid Mech. **635**, 103 (2009).
[25] M. Hultmark, M. Vallikivi, S. C. C. Bailey, and A. J. Smits, Turbulent Pipe Flow at Extreme Reynolds Numbers, Phys. Rev. Lett. **108**, 094501 (2012).
[26] M. Hultmark, A theory for the streamwise turbulent fluctuations in high Reynolds number pipe flow, J. Fluid Mech. **707**, 575 (2012).
[27] A. J. Smits, B. J. McKeon, and I. Marusic, High-Reynolds number wall turbulence, Annu. Rev. Fluid Mech. **43**, 353 (2011).
[28] M. Lee and R. D. Moser, Direct numerical simulation of turbulent channel flow up to $Re_\tau \approx 5200$, J. Fluid Mech. **774**, 395 (2015).
[29] J. Jiménez, Cascades in wall-bounded turbulence, Annu. Rev. Fluid Mech. **44**, 27 (2011).
[30] U. Högström, J. Hunt, and A. Smedman, Theory and measurements for turbulence spectra and variances in the atmospheric neutral surface layer, Boundary-Layer Meteorology **103**, 101 (2002).
[31] I. Marusic, On the role of large-scale structures in wall turbulence, Phys. Fluids **13**, 735 (2001).
[32] L. Agostini and M. Leschziner, On the influence of outer large-scale structures on near-wall turbulence in channel flow, Phys. Fluids **26**, 075107 (2014).
[33] L. Agostini and M. Leschziner, Predicting the response of small-scale near-wall turbulence to large-scale outer motions, Phys. Fluids **28**, 015107 (2016).
[34] L. Agostini, M. Leschziner, and D. Gaitonde, Skewness-induced asymmetric modulation of small-scale turbulence by large-scale structures, Phys. Fluids **28**, 015110 (2016).
[35] S. B. Pope, *Turbulent Flows* (IOP Publishing, 2001).
[36] M. Vallikivi, B. Ganapathisubramani, and A. Smits, Spectral scaling in boundary layers and pipes at very high Reynolds numbers, J. Fluid Mech. **771**, 303 (2015).